

Geochemistry, Geophysics, Geosystems®



RESEARCH ARTICLE

10.1029/2021GC009873

Special Section:

Insights into Subduction Zone Processes from Models and Observations of Exhumed Terranes

Key Points:

- Modified thermodynamic model accurately reproduces high-pressure sediment melting experiments relevant to subduction zone conditions
- Coupling this model to a dynamic model of sediment diapirism produces multiple outcomes, including relamination and deep subduction
- Model results show that relamination will dominate for greater sediment thicknesses, more felsic sediments, and warmer subduction zones

Supporting Information:

Supporting Information may be found in the online version of this article.

Correspondence to:

B. Z. Klein,
benjaminzachary.klein@unil.ch

Citation:

Klein, B. Z., & Behn, M. D. (2021). On the evolution and fate of sediment diapirs in subduction zones. *Geochemistry, Geophysics, Geosystems*, 22, e2021GC009873. <https://doi.org/10.1029/2021GC009873>

Received 29 APR 2021

Accepted 9 OCT 2021

On the Evolution and Fate of Sediment Diapirs in Subduction Zones

Benjamin Z. Klein^{1,2}  and Mark D. Behn¹ 

¹Department of Earth and Environmental Sciences, Boston College, Chestnut Hill, MA, USA, ²Now at Institute of Earth Science, University of Lausanne, Lausanne, Switzerland

Abstract At subduction zones, significant volumes of sediments and other crustal material are carried on top of the downgoing plate past the trench and into the mantle. This represents the dominant process by which material from the Earth's surface is recycled to the interior. However, the fate of these recycled materials is uncertain. Subducted material may be carried with the slab into the deep mantle, or it may form diapirs that ascend into the hotter portions of the mantle wedge, where they can melt and/or be relaminated to the base of the arc crust. While this material can be a mixture (or “mélange”) of sediments, oceanic crust and mantle rocks, here we focus on the dynamics of the uppermost layer of sediments on the downgoing slab. We modified a thermodynamic model to accurately predict the equilibrium mineral assemblage, melting behavior, and density of a range of subducted sediment compositions at pressure and temperature conditions relevant to subduction zones. Using this thermodynamic model, we constructed a coupled dynamic model of sediment diapirs and identified the primary parameters that control diapir behavior: sediment thickness and composition, and the thermal state of the subduction zone. Relamination of ascending diapirs is favored by greater sediment thicknesses, more felsic compositions, and warmer thermal conditions. By contrast, diapirism is suppressed in colder arcs, or where subducted sediment layers are thin or more mafic. Applying this model to modern subduction zones suggests that multiple processes are active today, with relamination occurring in a significant subset of modern arcs.

Plain Language Summary Sediments and other crustal material are dragged by downgoing plates into the Earth's mantle at subduction zones. The final fate of these materials is currently not known: the sediment may melt as the slab-top heats, rise into the hotter portion of the subduction zone mantle, or be dragged into the deep mantle. If sediment material is buoyant and rises into the hot core of the subduction zone mantle it may heat and begin to melt. Finally, buoyant material may rise through the mantle and be added to the base of arc crust. In this study, we developed a model to explore these processes and the stable minerals and melts produced by sediment material in subduction zones. Using this model, we find that the fate of sediments depend on the sediment composition and volume and on the temperature structure of the subduction zone. Warmer subduction zones, and large volumes of low density sediments create conditions favorable for sediments to rise into the mantle and be added to the overriding arc crust. In contrast, cold subduction zones, and smaller, denser sediment volumes results in sediments being carried into the deep mantle.

1. Introduction

Subduction of sedimentary material, combined with subduction erosion, is the dominant mechanism for returning differentiated continental material to Earth's mantle (Clift et al., 2009; Scholl & von Huene, 2007). The modern flux of crustal material to the mantle is estimated to be of the same order of magnitude as the present rate of continental addition at subduction zones (Clift et al., 2009), and at some convergent boundaries may outpace the addition of new continental material.

The presence of sedimentary material in both modern and ancient exposed accretionary complexes and subduction interfaces (Agard et al., 2018; Meneghini et al., 2009; Tewksbury-Christle et al., 2021), seismic observations consistent with fore-arc sedimentary material (Bassett et al., 2010; Scholl, 2019), and fore-arc uplift (Clift & Hartley, 2007; Riker-Coleman et al., 2006) all indicate that a portion of the sedimentary material delivered to subduction zones is removed from the slab and either accreted to or underthrust beneath the over-riding plate at fore-arc depths. Recent estimates at individual subduction zones suggest

© 2021. The Authors.

This is an open access article under the terms of the [Creative Commons Attribution-NonCommercial-NoDerivs License](https://creativecommons.org/licenses/by-nc-nd/4.0/), which permits use and distribution in any medium, provided the original work is properly cited, the use is non-commercial and no modifications or adaptations are made.

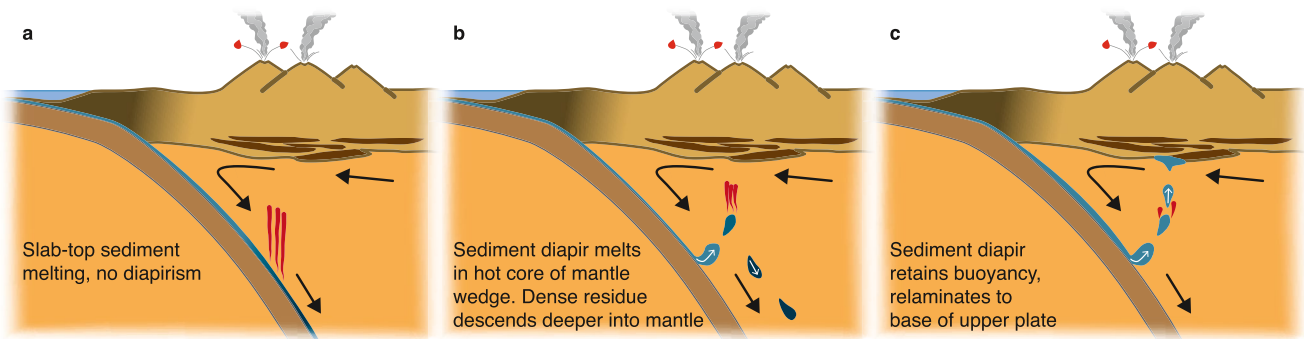


Figure 1. Cartoons illustrating the range of sediment behaviors proposed in subduction zones. Sediments may (a) melt or dehydrate along the slab top; (b) form diapirs that melt in the mantle wedge, and following melt extraction become negatively buoyant and sinking back into the mantle; or (c) form diapirs that either do not melt or do not melt sufficiently to become negatively buoyant and are relaminated to the base of the arc crust. Subduction zone cartoon modified from Jagoutz and Kelemen (2015).

that anywhere from 10% to 80% of trench sediments are removed from the slab by these processes (Agard et al., 2009; Clift & Hartley, 2007; Tewksbury-Christle et al., 2021). However, a recent compilation shows that while these processes likely reduce the global flux of sediments to the mantle by roughly 35% (Straub et al., 2020), they may be more than balanced by the addition of crustal material to the downgoing slab top by subduction erosion (Clift & Vannucchi, 2004; Straub et al., 2020). As such, the subduction of sediments and other crustal material past fore-arc depths plays a critical role in the global recycling of incompatible elements and isotopically evolved material (e.g., Chauvel et al., 2007; Scholl & von Huene, 2009).

The ultimate fate of sedimentary materials subducted beyond the fore-arc is uncertain. At least five different processes have been proposed for the fate of sediments as they are subducted: (a) sediments may partially melt and/or release hydrous fluids as they heat on the slab surface, with the residues transported with the slab to the deeper mantle (Figure 1a) (Elliott et al., 1997; Johnson & Plank, 1999; Plank & Langmuir, 1993); (b) sediments may form diapirs that partially melt as they rise into the hotter portions of the mantle wedge, producing a dense residue that descends back toward the slab (Figure 1b) (Behn et al., 2011; Cruz-Uribe et al., 2018; Marschall & Schumacher, 2012); (c) alternatively, if the sediment diapirs do not melt to significant extents, or remain buoyant during melting, this solid material may ascend through the mantle wedge and be emplaced at the base of the overriding arc crust, a process referred to as relamination (Figure 1c) (Currie et al., 2007; Hacker et al., 2011; Kelemen & Behn, 2016); (d) buoyant sediment may instead be exhumed via channel flow along the slab top (Erdman & Lee, 2014; Gerya et al., 2002; Guillot et al., 2009); and (e) the sediments may only minimally contribute to subduction zone processes and instead be advected with the slab directly to the deeper mantle (Chauvel et al., 2009).

Each of these processes is supported by combinations of geochemical and geophysical observations. While primary arc melts are dominantly basalts produced by melting the mantle wedge (Schmidt & Jagoutz, 2017), a range of trace element and isotopic data require that sediment-derived material contributes to these melts. Trace element signatures such as U/Th (Hawkesworth et al., 1997) and Th/La (Plank, 2005) ratios require contributions from sedimentary material to arc lavas. Similarly, the presence of cosmogenic ^{10}Be , which has a half-life of ~ 1.4 million years, in arc magmas unequivocally requires that recently subducted material originally at the Earth's surface contributes to at least some arc magmas (Morris et al., 2002). Finally, recent studies using the non-traditional stable isotopes systems of barium and thallium have found evidence for subducted sediment contributions to at least some arc magmas (Nielsen et al., 2016, 2020).

Multiple observations can be used to further differentiate between slab top melting and melting within buoyant diapirs. First, large ion lithophile element enrichments are considered a characteristic sediment signature in many arc lavas. However, these elements are strongly compatible in phengite, and therefore sediment melts will not be enriched in these elements until the breakdown of phengite (Johnson & Plank, 1999; Schmidt, 2015), which requires hotter temperatures than are predicted along slab top geotherms (cf., van Keken et al., 2018). Second, it has been observed that highly incompatible elements typically enriched in arc magmas (e.g., Th, Pb, and Nd) are only depleted in ultra-high pressure (UHP) sediments that record

temperatures in excess of 1,050°C (Behn et al., 2011). Finally, the absence of heavy rare earth element depletions in most arc magmas has been taken as evidence that melting of slab components must typically occur at pressures of at most 2 GPa, where melting residues are garnet-free (Nielsen & Marschall, 2017). Slab top geotherms at these relatively shallow depths are much colder than required by these observations, suggesting a component of sediment melting during ascent through the hot core of the mantle wedge.

In contrast to the abundant evidence for subducted sediment contributions to arc magmas, there is relatively limited observational evidence that requires relamination of sediment diapirs. The presence of old inherited zircons in arc lavas that could not have been acquired through assimilation of known upper plate sources may be indicative of sediment relamination (Gómez-Tuena et al., 2018). The close spatial association of felsic granulites and peridotites in the Bohemian Massif has also been suggested as diagnostic of relamination (Kusbach et al., 2015). Further, the structures and P-T paths documented for some UHP localities support diapiric exhumation consistent with relamination (Chatterjee & Jagoutz, 2015; Little et al., 2011), while the P-T paths from many other UHP localities instead indicate exhumation along a subduction channel (Agard et al., 2009; Ernst et al., 2007). Finally, recent observations of P-wave scattering due to seismic reflectors located above the Ryukyu slab are consistent with ~1 km buoyant diapirs within the mantle wedge (Lin et al., 2019, 2021). By contrast, seismic observations from the Aleutians and Marianas were used to argue that the vast majority of subducted sediments are carried beyond subduction zones to greater mantle depths, inconsistent with relamination (Horleston & Helffrich, 2012). Trace element and isotopic data from hot spot volcanism (Chauvel et al., 2007; Rapp et al., 2008) and MORBs (Nielsen et al., 2018; Rehkämper & Hofmann, 1997) also support the recycling of subducted sediment or residue components to the deeper mantle where they contribute to the formation of enriched mantle reservoirs.

Complementing these observations, a range of modeling studies have examined the behavior of subducting sediments. Kinematic-dynamic models of subduction zones provide estimates for steady-state slab-top temperatures (Syracuse et al., 2010; van Keken et al., 2018; Wada & Wang, 2009), and have been coupled with thermodynamic models to show where the sediment layer atop subducting slabs is likely to either dehydrate or melt (Hacker, 2008; van Keken et al., 2011; Wada et al., 2012). Another class of modeling studies has focused on the dynamic behavior of subducted material based on its density evolution (e.g., Gerya et al., 2003). These studies show that diapirs composed of buoyant sediments, hydrated peridotite, and/or *mélange* are likely to nucleate at sub-arc depths, prior to the onset of slab-top melting (Behn et al., 2011; Gerya & Yuen, 2003; Hasenclever et al., 2011), and either melt in the mantle wedge (Castro & Gerya, 2008; Castro et al., 2013; Gerya et al., 2006) or transit the wedge and relaminate to the base of the arc crust (Currie et al., 2007; Maierová et al., 2018; Maunder et al., 2016). A recent study examining the dynamics of melting within a sediment diapir showed that accounting for the depletion of the melting sediments can significantly reduce the total extents of melting, supporting the viability of relaminating sediment diapirs (Zhang et al., 2020).

However, none of these dynamic models of buoyant subduction zone diapirs incorporate detailed petrographic models that describe the changing mineralogy and density of the subducted sediments as they are subducted and melt. The relationship between melt productivity and temperature is strongly nonlinear for sediment compositions, particularly in open systems where melt-extraction occurs (Mann & Schmidt, 2015; Spandler et al., 2010), and the density of sediments can increase significantly following melt extraction (Hacker et al., 2011). Omitting these effects leads to uncertainty in the ultimate behavior and transport of sediments once diapirs have nucleated. This study addresses this question with two approaches. First, we modify existing thermodynamic phase equilibria models to better reproduce the experimentally observed melting behavior of sediments at sub-arc conditions and use this model to examine the melt production and buoyancy of a range of sediment compositions undergoing both equilibrium and near-fractional isobaric melting at 3 and 4 GPa. Second, we couple this modified phase equilibria model with a dynamic model of subduction zone diapirs. Using this coupled model, we show that a range of behaviors should be expected for diapirs depending on their composition, size, and the thermal conditions of the subduction zone.

2. Thermodynamic Modeling of Sediment Melts at Sub-Arc Conditions

2.1. Sediment Melting Experiments

The melting behavior of pelitic sediments at sub-arc conditions is well-characterized experimentally. Sub-solidus mineral assemblages at sub-arc slab top conditions (3–5 GPa) consist of coesite + jadeitic clinopyroxene + garnet ± kyanite ± phengite ± rutile ± carbonate (e.g., Poli & Schmidt, 2002; Schmidt et al., 2004). In this assemblage, phengite is the only major potassium bearing phase, and is also the only hydrous mineral. Thus, the maximum amount of structurally bound water that can be accommodated in a given bulk composition is fixed by the potassium content. The location of the solidus in CO₂-free sediment compositions is dictated by the hydration state of the sediment. The fluid-saturated solidus, marking the location of the first melt formed in the presence of a free fluid phase, is located between 700 and 750°C at 3 GPa and increases to between 790 and 850°C at 5 GPa (Hermann & Spandler, 2008; Mann & Schmidt, 2015; Nichols et al., 1994; Skora & Blundy, 2010). In the fluid-saturated system, phengite stability extends 100–200°C above the solidus and initial melt productivity increases with the amount of excess fluid. At pressures greater than ~5 GPa, the wet solidus terminates at the second critical point (Schmidt et al., 2004). By contrast, the fluid-absent solidus, where the only water in the system is bound in hydrous minerals (i.e., dehydration melting), is located at ~890°C at 3 GPa and 1,040°C at 4.5 GPa. In this system, phengite is destabilized at temperatures only slightly above the solidus (Mann & Schmidt, 2015), and this near-solidus phengite-breakdown melting produces melt fractions of 15%–30%. The anhydrous solidus occurs at significantly higher temperatures, and is located between 1,150 and 1,200 °C at 3 GPa and near 1,250°C at 5 GPa (Spandler et al., 2010). Near-solidus melts in all systems are silica-rich, and are granitic in the hydrous systems and dacitic in the anhydrous system. Finally, addition of CO₂ to the hydrous pelite system has a relatively minor effect on the solidus: the H₂O + CO₂ fluid-saturated solidus is ~30°C hotter than the H₂O only solidus (Skora et al., 2015), while the addition of CO₂ does not appreciably change the location of the fluid-absent solidus (Mann & Schmidt, 2015).

A modeling approach to sediment melting that explores the behavior of sediment diapirs should ideally satisfy multiple criteria: it should correctly predict the subsolidus mineral assemblage; accurately locate the solidus for a range of compositions and water contents; produce reasonable melt compositions and volumes; and finally, reproduce the decreasing melt fertility and increasing solidus temperature expected for sediments that have been depleted by previous melt extraction. To date, no existing model accomplishes all of these objectives. Current thermodynamic phase equilibria approaches (e.g., MELTS or THERMOCALC) were not developed to model sediment melting at pressures above 1–2 GPa. When extending these models beyond their calibrated ranges, they do not correctly locate the experimentally defined solidus and do not accurately predict melt compositions or melt fractions (Figure 2). Alternatively, a set of empirical models developed explicitly for the melting of sediments at sub-arc conditions reproduces experimentally observed average melt fractions (Mann & Schmidt, 2015) and compositions (Schmidt, 2015). However, these models were developed for low to moderate melt fractions when the melting reactions are buffered by the presence of phengite + clinopyroxene + garnet + coesite/quartz, and thus they cannot be used for open-system melting scenarios where the bulk composition becomes increasingly depleted.

2.2. Modified Sediment Melting Thermodynamic Model

Although no published models exist that are explicitly designed for the investigation of sediment melting at sub-arc conditions, we attempted to use existing activity-composition (a-X) models developed for use at lower pressures (Holland et al., 2018) to reproduce experimental studies of sediment melting at subduction zone conditions. Calculations were performed using *Perple_X* version 6.9.0 (Connolly, 2005; 2009; downloaded May 2020) in the system SiO₂-TiO₂-Al₂O₃-FeO-MgO-CaO-Na₂O-K₂O-H₂O. We included solution models for: olivine, orthopyroxene, garnet, biotite, and melt (Holland et al., 2018); omphacitic clinopyroxene (Green et al., 2007); clinoamphibole (Green et al., 2016); white mica and ilmenite (White et al., 2014); and feldspar (Holland et al., 2003). We focused on reproducing melting experiments in the fluid-absent (where all water is structurally bound) and anhydrous systems, as these are the conditions most likely found in sediment diapirs that have nucleated and detached from the subducted slab. Successfully modeling fluid-saturated melting behavior requires the ability to also model the sub-solidus fluid phase, which

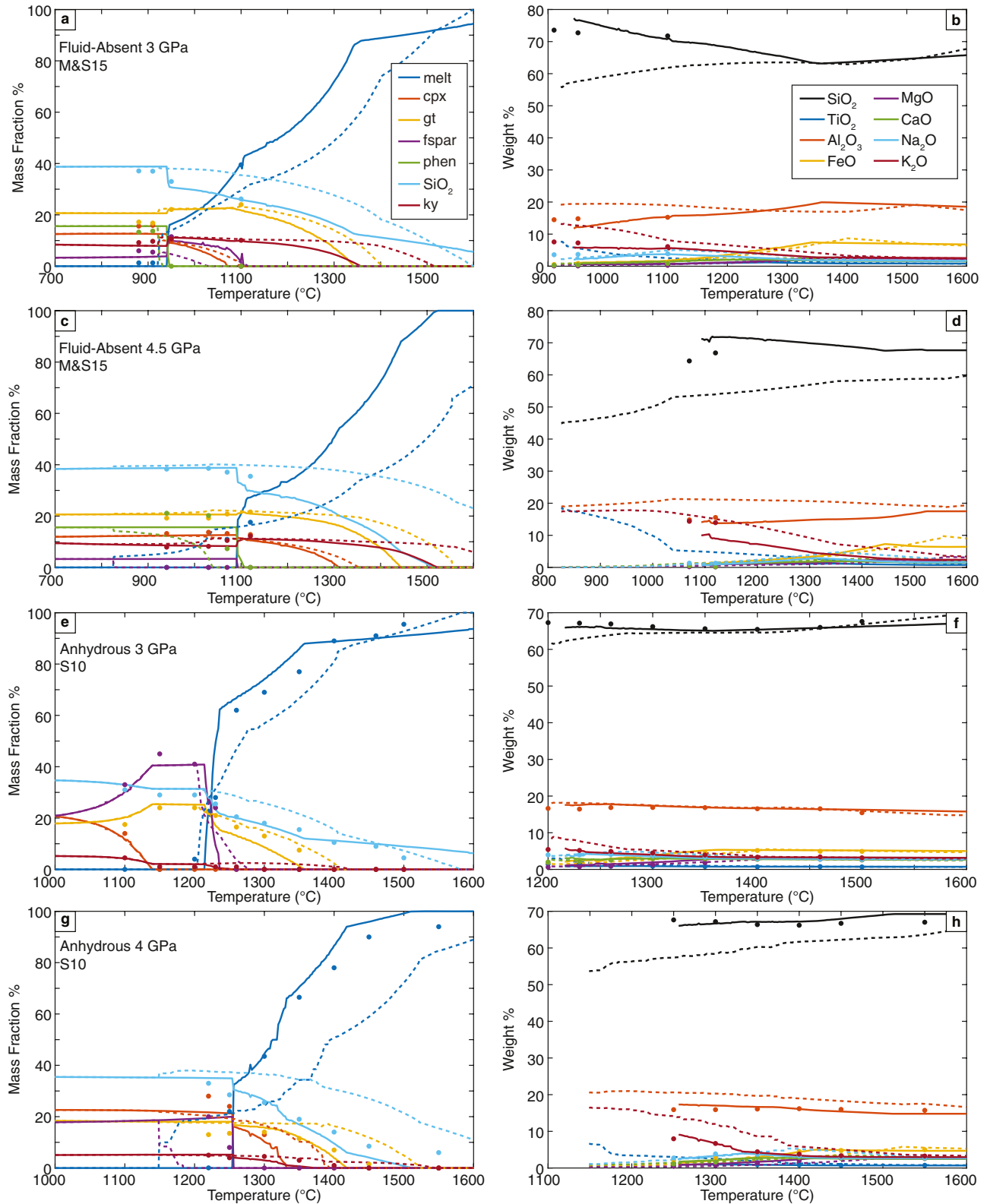


Figure 2.

at elevated pressures can have a significant dissolved silicate component (e.g., Manning, 2018). Although a solution model for such a phase is included in the Holland et al. (2018) models, it was not developed for use at pressures greater than ~2 GPa.

These models were not intended to be used at subduction zone pressures, and unsurprisingly do not accurately reproduce experimental observations. Specifically, in comparison to fluid-absent experiments (Mann & Schmidt, 2015), the modeled solidus is consistent with experiments at 3 GPa, but is located more than 200°C below the experimental solidus at 4.5 GPa (Figures 2a and 2c). Moreover, the modeled melt compositions near the solidus do not match the experimental data, predicting melts with less than 60 wt% SiO₂ and elevated Al₂O₃, TiO₂, and K₂O contents (all normalized anhydrous, Figures 2b and 2d). Similarly, in comparison to anhydrous sediment melting experiments (Spandler et al., 2010), the modeled 4 GPa solidus is more than 100°C below the experimental observation, melt production above the solidus is suppressed (Figures 2e and 2g), and predicted melt compositions are unrealistically silica poor (Figure 2h).

Based on these comparisons, we modified the Holland et al. (2018) melt a-X model to better reproduce sediment melting behavior at subduction zone conditions. As the published models successfully reproduce sub-solidus mineral assemblages (Figure 2), and these models have been used previously in studies of sub-solidus UHP metamorphism (e.g., Chapman et al., 2019), we did not modify any solid phase a-X models. We attempted to avoid overfitting the limited number of fluid-absent (Mann & Schmidt, 2015; Tsuno & Dasgupta, 2012) and volatile-free (Spandler et al., 2010) sediment melting experiments at pressures above ~3 GPa by manually making the minimum number of necessary modifications to the existing a-X model, and initially refined the model in the simpler anhydrous system, before extending the calibration to include H₂O. We primarily restricted adjustments to the published endmember enthalpy modification terms, but found that an adjustment of the mixing interaction term between the silica and H₂O endmembers was also necessary (Table S1 in Supporting Information S1).

Using this modified melt a-X model, performance relative to the experimental observations is much improved. The modeled fluid-absent and anhydrous solidi locations are consistent with experiments at 3 GPa and are overestimated by <25°C relative to higher pressure experiments (Figures 2a, 2c, 2e, and 2g). Melt compositions and solid residue mineralogy are also more consistent with experimental results; all initial melts are granitic in composition (Figures 2b, 2d, 2f, 2h), and the increased stability of potassium feldspar following phengite breakdown at 3 GPa is reproduced (Figure 2a). We also compared the modified a-X model to additional experimental studies that used tonalite (Patiño-Douce, 2005) and an anhydrous MORB bulk compositions (Klemme et al., 2002), and to sediment melting experiments at 2.4 GPa (Auzenneau et al., 2006) (comparisons included in Figure S1 of Supporting Information S1). Although these experiments were not included in our calibration data set and are outside of the calibrated composition and pressure range, the model successfully reproduces the major experimental melting systematics, suggesting that the modified a-X model is capable of modeling melting in a range of sediment compositions at ~2–5 GPa.

We caution that the modified a-X melt model was developed for sub-arc mantle wedge conditions, and that it is not benchmarked or intended for use significantly outside of the tested pressure range. Specifically, the original published hydrous melt model in Holland et al. (2018) was developed for use at pressures less than 2–2.5 GPa, and will perform better than our modified version at these conditions. Our model also does not incorporate the transition from silicate melt to supercritical liquid at >5 GPa, and therefore cannot be used at pressures greater than ~5 GPa. While the presence of Fe³⁺ can have a significant effect on phase equilibria and a Fe³⁺ melt endmember is present in the Holland et al. (2018) models, we did not attempt to recalibrate this component and instead excluded ferric iron from all calculations, as the Fe³⁺/Fe^{Total} ratios of slabtop materials, and also of most experimental minerals and liquids, are poorly constrained. Finally, as the original Holland et al. (2018), a-X melt model does not include CO₂ and MnO solution endmembers, we did not include these components in our recalibrated model, and therefore are unable to examine the melting behavior of either carbonate-bearing or MnO-rich sediments.

Figure 2. Comparison of sediment melting experiments (points) to the original Holland et al., (2018) thermodynamic model (dashed lines) and our modified a-X melt model (solid lines). The modified model better reproduces experimental equilibrium mineral assemblages, melt productivities, and melt compositions, for a range of bulk compositions and pressures for both fluid-absent and anhydrous conditions. Experiment abbreviations: M&S15: Mann and Schmidt (2015); S10: Spandler et al. (2010). Mineral abbreviations: cpx—clinopyroxene; gt—garnet; fspar—alkali feldspar; phen—phengite; SiO₂—quartz and/or coesite; ky—kyanite. Not shown—minor quantities of (Fe)Ti oxides.

Table 1
Bulk Compositions Used in Diapir Simulations and Melt-Depleted Sediment Residues

Composition	Mafic sediment ^a		Intermediate Sediment ^b			Felsic sediment ^c		Mantle ^d		
		R1	R2	–	R1	R2	–	R1	R2	–
Residue	–	R1	R2	–	R1	R2	–	R1	R2	–
<i>T</i> , °C	–	970	1,250	–	970	1,250	–	970	1,250	–
Total Melt Removed, wt%	0%	25%	46%	0%	23%	47%	0%	23%	50%	–
SiO ₂	54.99	48.41	44.55	63.28	60.18	57.66	67.49	65.71	65.67	45.69
TiO ₂	0.87	0.95	0.88	0.84	0.90	0.92	0.73	0.76	0.71	0.20
Al ₂ O ₃	17.35	19.67	19.05	16.81	18.44	18.78	14.72	15.74	14.81	3.35
Cr ₂ O ₃										0.41
MgO	3.51	4.52	6.01	3.24	3.99	5.23	2.23	2.70	3.58	38.68
FeO	7.73	10.10	13.18	6.46	8.13	10.57	5.12	6.31	8.31	8.12
CaO	8.64	11.09	13.81	2.64	3.16	3.20	3.44	4.11	4.30	3.15
Na ₂ O	2.61	3.03	2.51	3.12	3.47	3.19	2.68	2.95	2.39	0.41
K ₂ O	3.13	2.24	0.01	2.63	1.73	0.46	2.61	1.73	0.23	–
H ₂ O	1.19 ^e	0	0	0.99 ^e	0	0	0.99 ^e	0	0	–

Note. All compositions listed as normalized wt% (hydrous).

^aAleutian Green Clay (Plank & Langmuir, 1998). ^bAleutian Clastic Turbidite (Plank & Langmuir, 1998). ^cNicobar Turbidite (Plank & Langmuir, 1998). ^dAverage pyrolite composition (Ringwood, 1979). ^eInitial H₂O contents calculated assuming all K₂O is in phengite.

2.2.1. Sub-Arc Mantle Thermodynamic Model

To calculate the buoyancy of sediment compositions relative to sub-arc mantle, we also calculate the phase equilibria and density of a representative pyrolytic mantle composition (Table 1) at sub-arc mantle conditions. These calculations were performed in the system SiO₂-TiO₂-Cr₂O₃-Al₂O₃-FeO-MgO-CaO-Na₂O with the following solution models: olivine, clinopyroxene, orthopyroxene, garnet, and spinel (Holland et al., 2018); and plagioclase feldspar (Holland et al., 2003). For simplicity, we focus on melting of the sediment assuming that it is much more fusible than the surrounding mantle.

2.3. Isobaric Sediment Melting

To illustrate the range of melting behaviors resulting from different sediment compositions, we explored the variations in buoyancy and melt production during isobaric sediment melting at 3 and 4 GPa using previously compiled subduction zone sediment compositions (Plank & Langmuir, 1998). We assume that all compositions are initially fluid-free, with sufficient H₂O present to have all K₂O present as phengite, and exclude compositions with more than 5 wt% CO₂ or 2 wt% MnO. Melting was modeled as either closed-system equilibrium melting, or fractional melting, where any present melt was removed at each modeled temperature node in *Perple_X* (final node spacing <1°C). This isobaric melting process emulates the initial heating of slabtop material along the slab top and in the steep thermal gradient immediately above the slab surface. Subsequent melting during diapiric ascent will be strongly sensitive to the buoyancy of individual sediment compositions and is considered in detail in Section 4.

At 3 GPa, bulk densities at temperatures below ~850°C range from 3,000 kg/m³ to ~3,400 kg/m³, and all but two of the modeled compositions are less dense than the sub-arc mantle (Figure 3a). With increasing temperature at 3 GPa, the system leaves the coesite stability field before crossing the solidus, stabilizing quartz, and causing the bulk density to decrease by between 25 and 200 kg/m³, proportional to the abundance of coesite/quartz in each composition. With further increases in temperature, all compositions cross the solidus between 900 and 1,000°C and rapidly produce between 5% and 25% melt (Figure 3b).

Above the solidus, both the density and the melt productivity of the fractional and equilibrium melting cases markedly diverge. As temperature increases, melt fraction continuously increases for all compositions in the equilibrium melting case. The bulk density (melt + residue) also decreases continuously in this

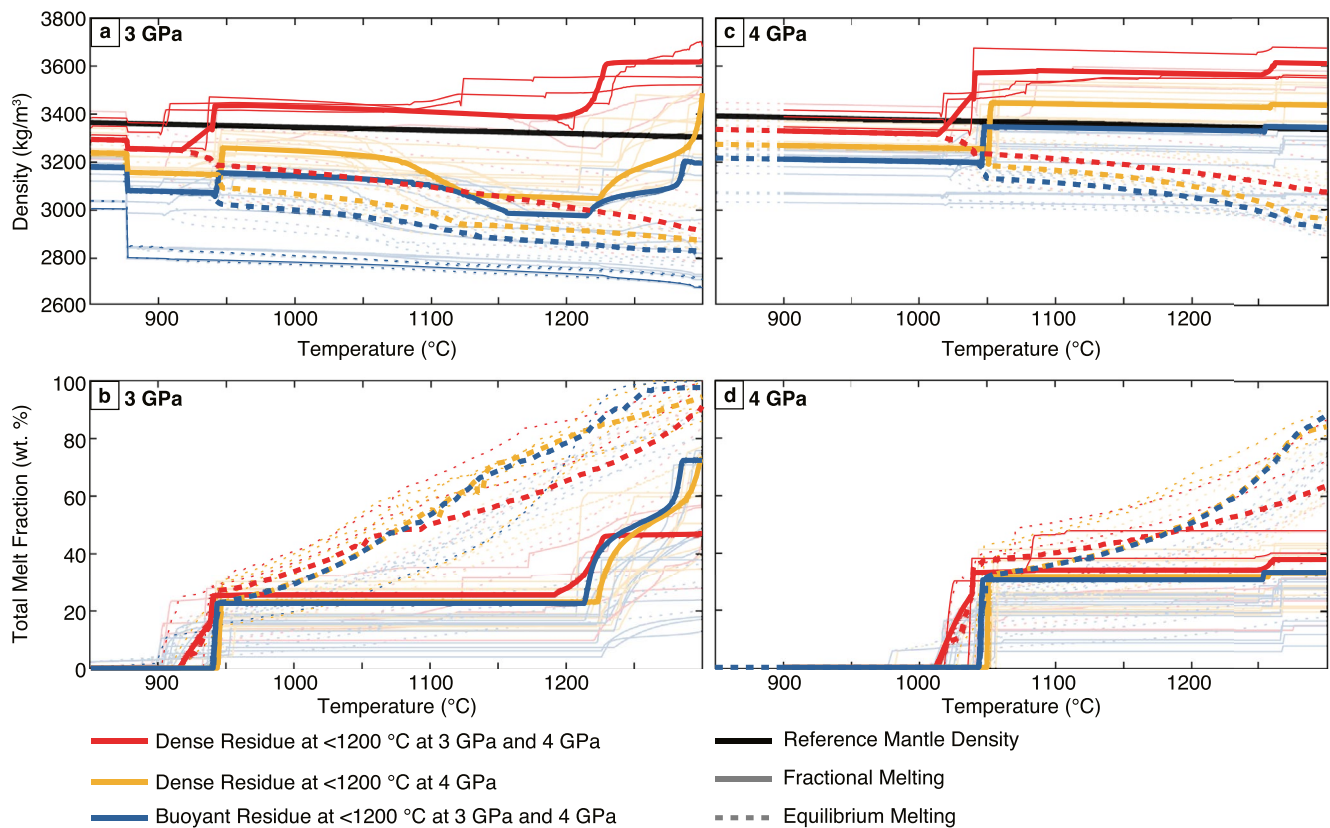


Figure 3. Melt productivity and density evolution along isobaric melting paths at 3 and 4 GPa for compiled subduction sediment compositions from Plank and Langmuir (1998). Solid lines show evolution during fractional melting, while dashed lines show equilibrium melting. Black line in panels (a) and (c) shows the density of ambient sub-arc mantle. Line color corresponds to buoyancy of sediments: blue lines represent sediments that produce buoyant solid residues relative to ambient mantle at all temperatures below 1,200°C at both 3 and 4 GPa; yellow lines show sediments that produce negatively buoyant residues at 4 GPa below 1,200°C but not at 3 GPa; red lines show sediments with negatively buoyant residues below 1,200°C at both 3 and 4 GPa. Thicker lines correspond to the felsic (blue), intermediate (yellow), and mafic (red) sediment compositions used throughout subsequent models.

scenario, as the melt component is significantly less dense than the solid residue. By contrast, following the initial near-solidus melting interval, the density of all compositions increases in the fractional melting scenario as melt extraction leaves a phengite-free residue. This residue is anhydrous and K_2O -poor, and does not melt further until temperatures above 1,200°C. At these high temperatures, further melting proceeds as the remaining K-feldspar breaks down. This further melting produces a maximum total melt fraction of 15%–65% at 1,300°C and significantly denser residues that range from 3,200 to >3,600 kg/m³.

Isobaric melting at 4 GPa follows a similar pattern to melting at 3 GPa. At this pressure, coesite is the stable SiO_2 -polymorph at all relevant temperatures and sub-solidus densities range from 3,050 to 3,450 kg/m³ with few compositions denser than ambient mantle (Figure 3c). The solidus is crossed in all compositions between 1,000 and 1,050°C, producing 5%–40% melt (Figure 3d). In the equilibrium melting case, continuous melting occurs above the solidus, with melt fractions increasing to >60% in most compositions by 1,300°C. This increase in melt fraction results in continuously decreasing bulk density. Similar to the 3 GPa case, near-solidus fractional melting leaves an anhydrous residue that does not undergo further melting until the temperature increases to at least 1,250°C. Above the 4 GPa solidus in the fractional melting case, the density of the residue of each composition increases and many compositions have densities comparable to or denser than the ambient mantle.

While the solidus and subsequent melting intervals are relatively invariant between compositions, the buoyancy of each composition is determined by its modal mineralogy and melt production, which are functions of bulk composition. SiO_2 contents exert the strongest control on bulk density (Figure 4). SiO_2 contents correspond to the quantity of coesite (or quartz) stable, which are the two least dense anhydrous silicate

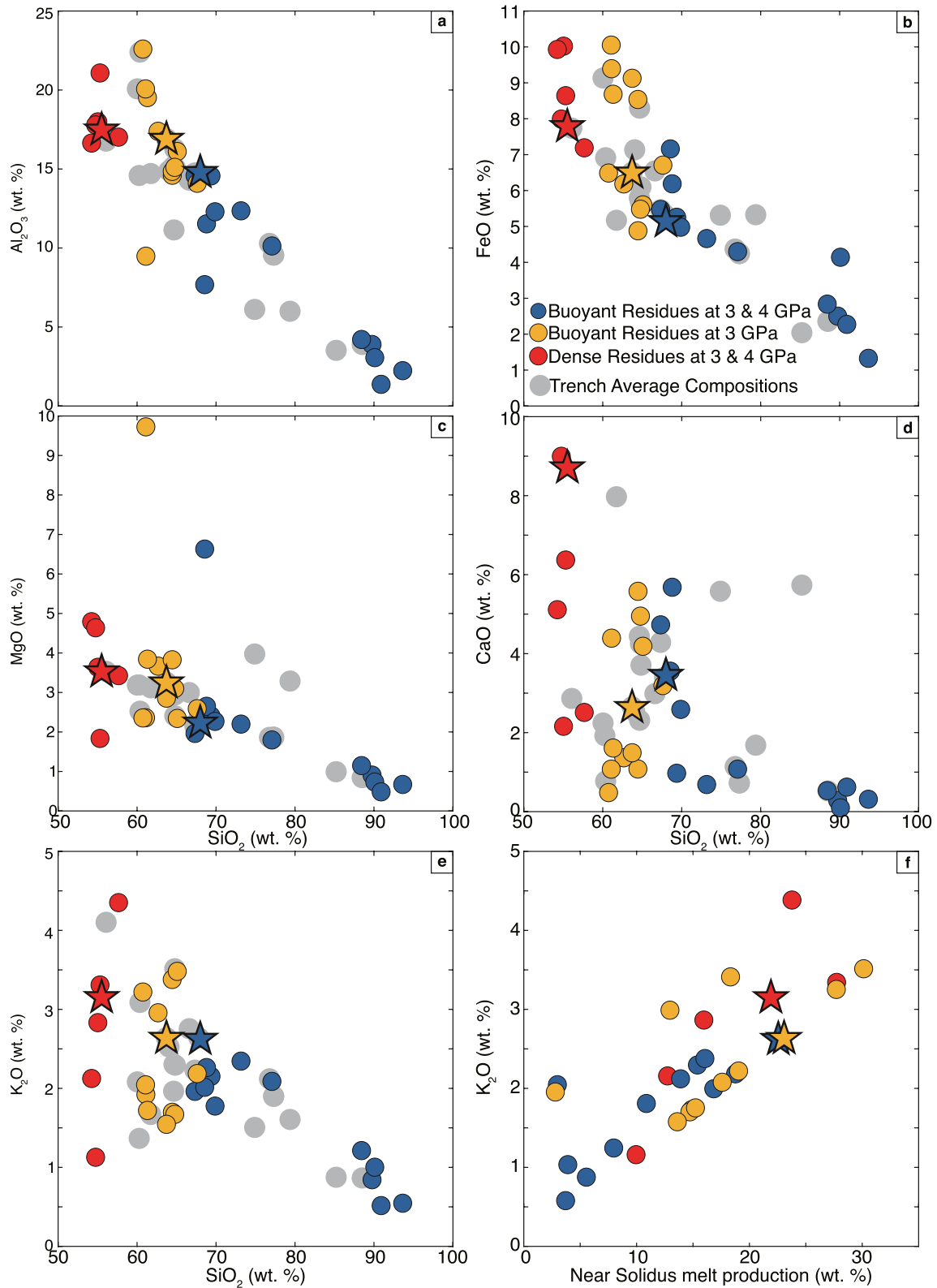


Figure 4.

phases present in sediments at slab-top conditions. Similarly, Al_2O_3 and FeO contents are correlated with garnet abundance and thus are inversely correlated with residue density (Figures 4b and 4d). Residue density is less sensitive to other components including MgO, CaO (Figures 4a and 4e), and Na_2O (not shown). Finally, because phengite is the only hydrous phase present in typical sediment compositions at slab-top sub-solidus conditions, bulk K_2O contents fix the maximum amount of water present at fluid-absent conditions (e.g., Hacker, 2008). As a result, K_2O contents are the primary control on near-solidus melt production (Figure 4f). However, the density of residues is not strongly controlled by the bulk K_2O contents (Figure 4e), and is also relatively insensitive to the initial melt productivity (Figure 4f).

As the buoyancy of different sediment compositions varies systematically with changes in composition, we focus the remainder of our study on three endmembers representative of comparatively mafic, intermediate, and felsic sediments (Figure 4 and Table 1). The most mafic sample we include is an Aleutian green clay from DSDP-183 (Plank & Langmuir, 1998), which likely has a mafic volcanoclastic component. We consider a composite composition of clastic turbidites also sampled from DSDP-183 as an intermediate composition (Plank & Langmuir, 1998), and to represent more silicic compositions we include a composition representative of the Nicobar Fan turbidites. These three compositions range from 51 to 64 wt% SiO_2 (normalized anhydrous), and encompass the bulk of the major element compositional variability present in subducted sediment, excluding carbonate-rich sediments and cherts (Figure 4). While these individual compositions represent distinct subducted sediment lithologies, and thus are not representative of bulk subducted sediment within a given subduction zone, we use these compositions to explore the range of behaviors produced by sediment diapirs. We observe that estimates for bulk subducted sediment compositions, both globally and at individual arcs (Plank & Langmuir, 1998), mostly occupy a restricted compositional space compared to our three compositional endmembers, and dominantly fall between the intermediate and felsic compositions (Figure 4). As we use these compositions only as representative endmembers, we primarily refer to them as mafic, intermediate and felsic sediments in the remainder of this work.

2.4. Buoyancy of Melt-Depleted Residue Compositions

A critical feature of the evolving composition and buoyancy of sediments undergoing fractional melting is that extraction of the initial hydrous melt produced by phengite breakdown results in an anhydrous refractory residue (Figure 3). This residue does not melt further until heated to significantly higher temperatures. However, the residues produced by most sediment lithologies following phengite breakdown are still buoyant relative to ambient mantle (Figures 3a and 3c). Therefore, diapir formation and ascent should be favorable even if phengite breakdown and melt extraction occurs near the slab-top. As these diapirs ascend into the hotter portion of the mantle wedge, further melting is possible at a range of P-T conditions.

To fully characterize the evolution of sediment buoyancy with changing pressure and temperature, we calculate the density difference between each of the three representative sediment bulk compositions (residue + melt) and the ambient mantle as a function of pressure and temperature (Figures 5a–5c). We then repeat this calculation for two sets of residues produced by fractional melting of each protolith to show how the buoyancy and melt productivity evolves with increasing extents of melting. Specifically, we show residues produced by isobaric fractional melting to 970°C at 3 GPa, just above phengite breakdown (Figures 5d–5f), and to 1,250°C at 3 GPa, approaching temperatures found in the hot core of the mantle wedge (Figures 5g–5i; temperature profiles through core of representative mantle wedges shown in Figures 5a–5c). We refer to these two sets of residues as R1 and R2 residues, and list their bulk compositions in Table 1. Interpreted pseudosections for all modeled compositions are included in Figure S2 of Supporting Information S1.

Above ~2 GPa, all three protolith compositions form sub-solidus mineral assemblages dominated by garnet + clinopyroxene + quartz/coesite + phengite that are buoyant relative to the ambient mantle

Figure 4. Compositional dependency of sediment buoyancy and melt productivity. (a–e) Harker plots showing the strong correlations between residue buoyancy and protolith SiO_2 , Al_2O_3 , FeO, and MgO content and only weak correlations with CaO and K_2O . (f) A strong correlation is present between protolith K_2O content and near solidus melt production, calculated as melt produced within 25°C of the solidus during 3 GPa fractional melting, but this is not well correlated with residue density. Estimates of bulk trench sediment composition from Plank and Langmuir (1998) shown in gray, other symbol colors as in Figure 3. Compositions used in Figure 5 and subsequent diapir models are marked with stars.

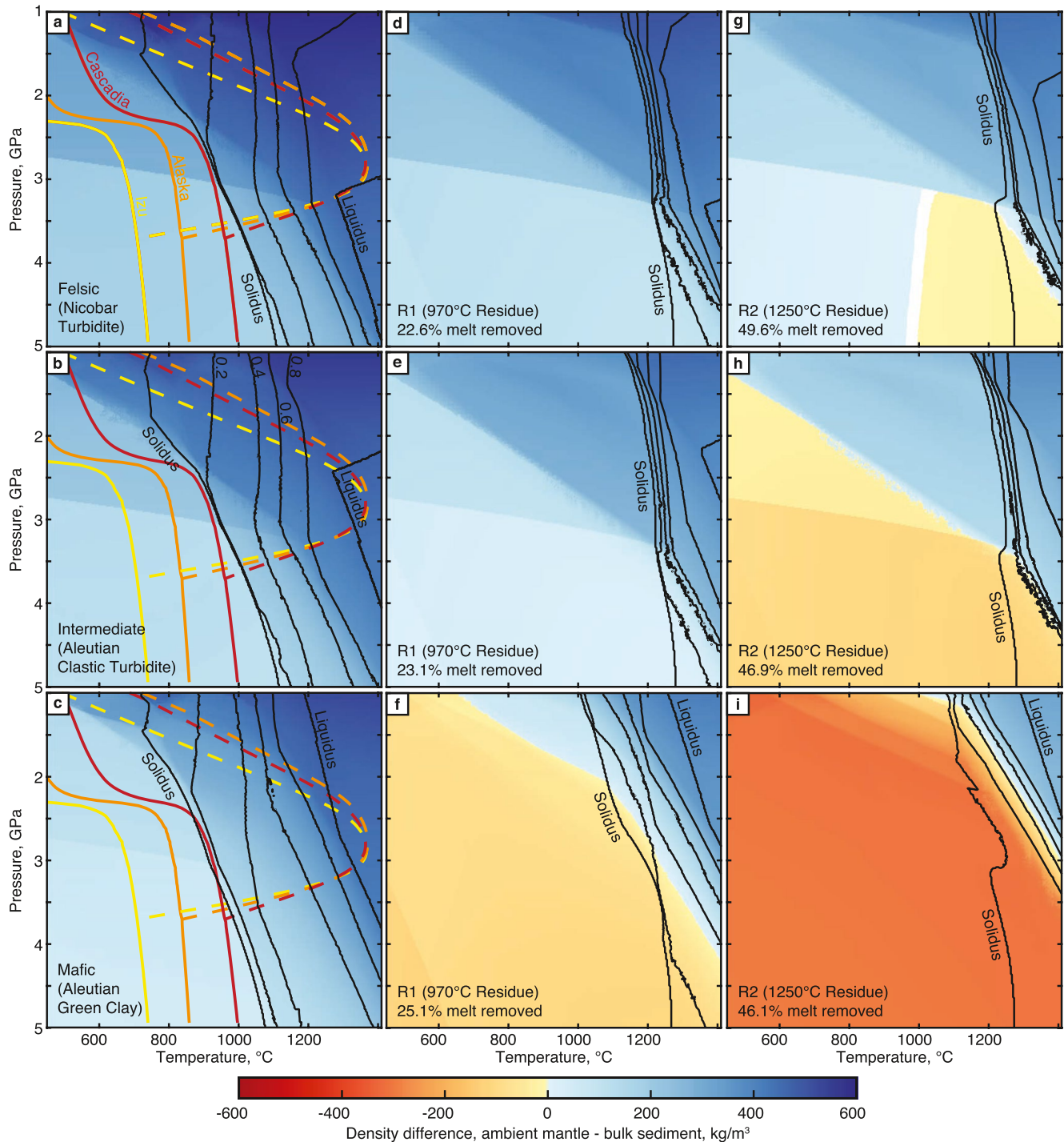


Figure 5. Density difference (ambient mantle—bulk sediment) maps as a function of pressure and temperature. Left column shows unmelted sediment protolith compositions. Middle and right columns show sediment residues formed by 3 GPa fractional melting to 970°C (R1) and 1,250°C (R2). Modeled melt fractions are plotted in black contours and mark 20% melt intervals. Panels (a–c) include slab top geotherm P-T paths from van Keken et al. (2018), including modifications described in text (solid lines) and temperature profiles along a vertical path through the mantle wedge originating at the slab top at 3.5 GPa depth (dashed lines). Figure S2 shows corresponding bulk sediment density maps, and also labels key mineral stability boundaries.

(Figures 5a–5c and Figure S2 in Supporting Information S1). During closed-system, equilibrium melting, ~20% melt is rapidly produced near the solidus, after which melt fractions increase continuously in all compositions as temperature increases, reaching the liquidus at temperatures above 1,200°C (Figures 5a–5c). Phengite is rapidly exhausted in all compositions above the solidus. With further increasing temperatures, additional phases melt out: quartz and coesite are exhausted ~100°C above the solidus in the mafic protolith, and with progressive melting at higher temperatures (at least 1,200°C), kyanite, clinopyroxene and garnet are fully exhausted in all compositions. During these melting reactions, the bulk density of all three compositions is always buoyant relative to the ambient mantle, as the retained melt reduces the bulk density (Figures 5a–5c). Moderate to cold slab top geotherms are >100°C below the solidi of all compositions. The hottest slab top geotherms (i.e., Cascadia) do not intersect the solidi of the intermediate and felsic compositions, but cross the mafic sediment solidus by less than 50°C at pressures between 2.5 and 3 GPa. At these conditions, the mafic sediment produces small melt fractions (~10%) without fully exhausting phengite.

The R1 compositions represent residues produced after isobaric fractional melting at 3 GPa to 970°C, corresponding to 22%–25% melt extraction. These residues are H₂O-free, and are denser at sub-solidus conditions compared to their unmelted protoliths. The mafic R1 residue dominantly forms a garnet-clinopyroxene-potassium-feldspar assemblage at sub-solidus conditions that is negatively buoyant relative to the mantle (Figure 5f and Figure S2 in Supporting Information S1), while the intermediate and felsic R1 compositions additionally stabilize significant quantities of quartz/coesite (20%–30%) and remain less dense than ambient mantle (Figures 5d and 5e). These anhydrous residues have significantly elevated solidi temperatures compared to their protoliths; further melting does not occur in any of the three compositions until temperatures exceed 1,200°C. These solidi are more than 200°C hotter than even the hottest slab top geotherms. However, vertical temperature profiles through the mantle wedge (dashed curves Figures 5a–5c), which are comparable to diapir ascent paths modeled in Section 4, indicate that sediment diapirs could experience temperatures above these solidi while ascending through the hot core of the mantle wedge in all subduction zones. Melt fractions in each R1 composition increase rapidly above the solidi, particularly in the felsic and intermediate compositions. Above the solidus, the increasing melt fraction causes all three R1 bulk assemblages to become less dense than the ambient mantle.

Finally, if we consider the refractory R2 residues produced by fractional melting to 1,250°C (~45%–50% melt removed), all three compositions are denser than ambient mantle at both sub-solidus and melt-present conditions. As the melting reactions above the anhydrous solidus are continuous and all three compositions still contain minor to trace amounts of K₂O, the stable mineral assemblages formed by these residues mirror those modeled for the R1 assemblages (Figure S2 in Supporting Information S1). However, the additional extracted melt results in significantly denser bulk assemblages compared to the R1 assemblages. The mafic R2 composition is silica-undersaturated, and stabilizes a garnet-rich nearly bimineraleclogite assemblage, which also includes minor corundum, hercynite, olivine and feldspathoids (Figure S2 in Supporting Information S1). This assemblage is denser than mantle at almost all conditions considered, and produces extremely high densities (>3,600 kg/m³, Figure S2 in Supporting Information S1) over a wide range of P-T conditions. The intermediate R2 composition also is negatively buoyant over a wide range of P-T conditions, and is only expected to be buoyant at less than 4 GPa and relatively high temperatures. Finally, the felsic R2 composition is denser than the ambient mantle in a restricted region at pressures above 3 GPa and temperatures above 1,000°C. However, even in this region, the felsic R2 composition is only slightly denser than the ambient mantle (<15 kg/m³). The solidi for all three compositions are located just above 1,250°C, consistent with the continuous melting reactions in these refractory compositions. Melting immediately above the solidi of these highly depleted residues is limited to melt produced during the breakdown of the small volumes of potassium-feldspar. Further melting requires temperatures of at least ~1,300°C, extremely high temperatures that are only present in the hottest portions of the mantle wedge.

3. Coupled Model of Diapir Melting and Ascent

3.1. Model Design

The thermodynamic model results described above show that the density of sediments varies greatly as they heat and melt at sub-arc conditions. With progressive fractional melting, many compositions transition from being positively to negatively buoyant relative to the ambient mantle. However, further complications

exist: diapirs will not melt at a single pressure, and thermal gradients will be present within a diapir as it heats while ascending through the mantle wedge, resulting in variable extents of melting and depletion within the diapir (Zhang et al., 2020). Thus, even as the exterior of a diapir melts and becomes denser than the mantle, it is possible that the diapir as a whole will remain positively buoyant. To model the evolution of sediment diapirs and determine what parameters are the dominant controls on diapir behavior, we coupled our recalibrated thermodynamic model with a dynamic model that simulates the advection and thermal evolution of a spherical diapir in the convecting mantle wedge.

The dynamic model we employ makes a number of simplifying assumptions. We assume that the background mantle temperature and flow fields are at steady state, and that the diapir is advected as a buoyant tracer within this field. That is, we assume that the diapir does not meaningfully modify the flow and temperature of the surround mantle wedge. This assumption is valid for the relatively small diapirs predicted to arise from typical subducting sediment layers (Behn et al., 2011; Miller & Behn, 2012). Additionally, we assume that the diapir is spherical and initially has a single composition.

These assumptions allow for a simplified approach: the diapir velocity is calculated by combining steady-state mantle wedge corner flow components (from van Keken et al., 2018) with a buoyancy-driven diapir component, while the temperature within the diapir is updated by solving the radially symmetric heat equation coupled to the thermodynamic model. Given these simplifying assumptions and uncertainties relating to the thicknesses and compositions of subducted sediment, our initial goal is to identify the dominant controls on subduction zone diapir behavior. Specifically, we model the behavior of diapirs composed of the representative mafic, intermediate, and felsic sedimentary protoliths (discussed above) in three different subduction zones: Izu, Alaska, and Cascadia, which are broadly characteristic of cold, moderate, and hot subduction zones, respectively (Wada et al., 2009). Following this treatment, we apply our model to modern subduction zones using best estimates for the sediment compositions and thicknesses and corresponding subduction zone thermal models.

The expected size of sediment diapirs at modern subduction zones is a function of subducted layer thicknesses (150–1,200 m: Clift & Vannucchi, 2004; Clift et al., 2009; Scholl & von Huene, 2007). Layer thicknesses can be related to diapir radii given the assumption that diapirs nucleate as optimally spaced Rayleigh-Taylor instabilities (Zhang et al., 2020) with wavelength (λ) equal to $2\pi h / k$ (Jull & Kelemen, 2001), where h is the sediment layer thickness and k is the non-dimensional wave number. For quartz-dominated sediment layers, k is approximately 0.5 based on non-Newtonian scaling analyses (Miller & Behn, 2012). Then, assuming that diapirs nucleate from a volume with horizontal dimensions λ and height h , the radius r can be estimated as $r = h\sqrt[3]{12\pi}$ (Zhang et al., 2020). Given this scaling relationship, expected sediment diapir radii range from ~0.5 to 4.0 km, which we take as the range of diapir radii examined in our models.

Finally, we consider the importance of varying the melt extraction threshold, from a near-fractional melting scenario (1%) to a closed, equilibrium melting scenario (i.e., 100%). We use a 1% threshold rather than an ideal fractional melting case for numerical stability, as on occasion `Perple_X` minimizations incorrectly generated small melt fractions below the fluid-absent solidus. However, because large melt fractions are expected to be produced immediately above the fluid-absent solidus, this 1% threshold effectively functions as true fractional melting. While it has been argued that melt extraction in these systems should be efficient (e.g., Schmidt, 2015), we note that there are numerous uncertainties in modeling melt velocities in a system with highly variable melt permeability, and also that large extrapolations are required to calculate both melt density and viscosity at the high pressures considered here. Further, sediment diapirs will be significantly more fusible compared to the surrounding mantle, which will generate sharp permeability gradients at the diapir margin. These sharp gradients may limit the efficiency of melt extraction from the diapir (Zhang et al., 2020). Finally, it is not clear that melt extraction will be favored given the modeled rapidly ascending diapirs (see below). To account for these uncertainties, we also examined diapir behavior with intermediate degrees of melt extraction, represented by melt extraction thresholds of 7, 20, and 50 vol%. The two lower values correspond to the liquid percolation and melt escape thresholds of Vigneresse et al. (1996), both of which are often invoked as melt extraction thresholds in crustal migmatites (Rosenberg & Handy, 2005), while the 50% threshold is likely less geologically relevant and is included to illustrate the behavior of open systems with higher melt extraction thresholds.

3.2. Diapir Velocity

The mantle flow velocity component is found by interpolating from a modified version of the steady-state subduction zone models published in van Keken et al. (2018), which are an update of previously published models (Wada & Wang, 2009). The models used here are identical to the published version with the exception that they use a mantle potential temperature of 1,350°C rather than 1,421.5°C (recalculated models provided courtesy of Dr. Ikuko Wada). This modification was made to be more consistent with typical estimates of modern mantle potential temperatures which range from ~1,300 to 1,400°C at modern subduction zones (e.g., Till, 2017) and from 1,280 to 1,400°C at mid-ocean ridge settings (e.g., Herzberg et al., 2007). These kinematic-dynamic models use fixed modern subduction zone geometries and prescribe the downgoing slab velocity and upper plate thickness. The models impose a fixed coupling depth of 75 km, where the interface between the downgoing slab and the overlying mantle material transitions from decoupled to fully coupled. Based on this kinematic forcing, the model solves for the velocity and temperature fields within the mantle wedge using a realistic wet olivine rheology. Finally, the models impose a 0.3°C/km adiabatic temperature gradient and include radiogenic, frictional, and viscous heating terms. These models were shown to be consistent with observations at modern subduction zones such as surface heat flow measurements (Wada & Wang, 2009).

The x and y mantle velocity components from the kinematic-dynamic model are added to a vertical buoyancy component to calculate the total diapir velocity. The buoyancy-driven component (V_d) is calculated using a modified version of the Stokes velocity equation that incorporates a temperature-dependent, power-law viscosity (Weinberg & Podladchikov, 1994; as modified by Burov et al. [2003]),

$$V_d = C \frac{\frac{1}{3}(\Delta\rho gr^2)}{\eta_{eff}} \quad (1)$$

where $\Delta\rho$ is the density difference between the ambient mantle and the average density of the diapir, both calculated using `Perple_X`, g is the gravitational acceleration, r is the diapir radius, and η_{eff} is the effective viscosity of the surrounding mantle. C is a function of the viscosity contrast between the diapir and the surrounding mantle, and can only range from 1 when $\eta_{mantle} \gg \eta_{diapir}$ to 2/3 when $\eta_{mantle} \ll \eta_{diapir}$. As the diapir velocity is only very weakly dependent on this variable, we assume for simplicity that $C = 1$ in all models.

In the original formulation of Weinberg and Podladchikov (1994), η_{eff} was calculated based on the local stresses generated by the buoyancy of the diapir. However, previous work has shown that the growth of Rayleigh-Taylor instabilities is influenced by the competing roles of background viscosity and local stress-controlled viscosity (Houseman & Molnar, 1997; Miller & Behn, 2012). Therefore, we modified the calculation of η_{eff} to be set by the smaller of η_{wedge} , the background viscosity of the mantle wedge, and η_{stokes} , the local stress-controlled viscosity surrounding the buoyant diapir:

$$\eta_{eff} = \min(\eta_{stokes}, \eta_{wedge}) \quad (2a)$$

Here, the mantle wedge viscosity is calculated assuming a wet olivine rheology based on the background strain rate $\dot{\epsilon}$ associated with corner flow and the subduction zone temperature structure:

$$\eta_{wedge} = \frac{3}{2} \frac{n+1}{2^n} \left(\frac{A}{2}\right)^{\frac{1}{n}} \exp\left(\frac{Q}{nRT}\right) \dot{\epsilon}^{\frac{1-n}{n}} \quad (2b)$$

where n is the stress exponent, Q is the activation energy, R is the ideal gas constant, T is temperature, and A is an experimentally determined constant. Rheological variables are set assuming a wet olivine flow law (Hirth & Kohlstedt, 2003), and are listed in Table 2.

Following Weinberg and Podladchikov (1994) and Burov et al. (2003), the stress-controlled viscosity associated with diapir ascent generated is calculated:

$$\eta_{stokes} = \frac{\left[6^{n-1} \exp\left(\frac{Q}{RT}\right)\right]}{3^{\frac{n-1}{2}} A (\Delta\rho gr)^{n-1}} \quad (2c)$$

Table 2
List of Variables Used in Diapir Simulations

Symbol (units)	Parameter	Value	Reference
Dynamic variables			
Q (kJ mol ⁻¹)	Activation energy	480	H&K2003 ^a
n	Stress exponent	3.5	H&K2003
A (MPa ⁻¹ s ⁻¹) ^b	Empirical constant	8.06e5	H&K2003
$\dot{\epsilon}$ (s ⁻¹)	Background strain rate	10⁻¹³ , [10 ⁻¹⁴ , 10 ⁻¹⁵] ^c	
$\Delta\rho$ (kg/m ³)	Density difference	Perple_X Calculated	
r (km)	Diapir radius	[0.5], 1, 2, 3, 4 ^d	
T_p (°C)	Mantle potential T	1,350	
R (J K ⁻¹ mol ⁻¹)	Gas constant	8.314	
g (m/s ²)	Gravitational acceleration	9.81	
V_d (m/s)	Diapir velocity	Calculated	
Heat equation variables			
C_p (J K ⁻¹)	Heat capacity	Perple_X calculated	
ρ (kg/m ³)	Density	Perple_X calculated	
C_p^{eff} (J K ⁻¹)	Eff. heat capacity	Perple_X calculated	
k (W m ⁻¹ K ⁻¹)	Thermal conductivity	Calculated	N2010 ^e
	Melt extraction threshold	1, 7, 20, 50, 100	

^aHirth and Kohlsted (2003). ^bA calculated for wet olivine as $A = \alpha^*(C_{OH})^r$, with $C_{OH} = 5000 \text{ H}/10^6 \text{ Si}$, $r = 1.2$ and $\alpha = 30$.
^cAll examples in main text shown with $\dot{\epsilon} = 10^{-13}$. Effect of other values of background strain rate shown in Figure S3.
^dResults in text primarily shown for 1–4 km radius diapirs, additional calculations with other radii were made to complete the regime diagrams shown in Figures 10 and 11. ^eNabelek et al. (2010).

For $n = 3.5$, η_{wedge} dominates in the slab-top region, while η_{stokes} rapidly becomes the dominant (i.e., weaker) viscosity term as the diapir rises above the slab surface into the warmer mantle wedge. Appropriate strain rates in the slab top region are difficult to constrain due to complexities associated with the rheology of mixtures of hydrous phases, variations in coupling along the plate interface, and smaller-scale dynamic effects associated with diapir nucleation not captured in the kinematic-dynamic models. As these complexities are not included in our modeling approach here and are absent from the kinematic-dynamic models that we use for background mantle velocity, we assume a constant, relatively high background strain rate of 10^{-13} s^{-1} to calculate η_{wedge} in all models. We evaluate the significance of this assumption in Section 5.5.1. Finally, the length of each timestep is calculated so that the diapir is never advected more than 1 km in a single timestep. Shorter timesteps were explored and did not meaningfully alter the results.

3.3. Radial Heat Equation

Following each advection step the temperature, density, and composition of the diapir are updated. We solve the radial heat equation (Equation 3) within the diapir using an implicit finite difference formulation:

$$\frac{DT}{Dt} = \frac{k}{\rho C_p^{eff}} \left(\frac{\partial^2 T}{\partial r^2} + \frac{2}{r} \frac{\partial T}{\partial r} \right) \quad (3)$$

where T is temperature, ρ is density, k is thermal conductivity, and C_p^{eff} is the effective heat capacity. At each time step, the material properties on each node are calculated iteratively with Perple_X, as well as a temperature-dependent k (Nabelek et al., 2010). Latent heat of fusion is accounted for in a thermodynamically consistent manner by iteratively calculating C_p^{eff} (Voller et al., 1990) as the local temperature derivative of enthalpy directly from the Perple_X output. The heat equation is solved with 100-m initial node spacing. Because melt-production, and thus effective heat capacity, are often strongly nonlinear and can increase abruptly near the solidus, we radially

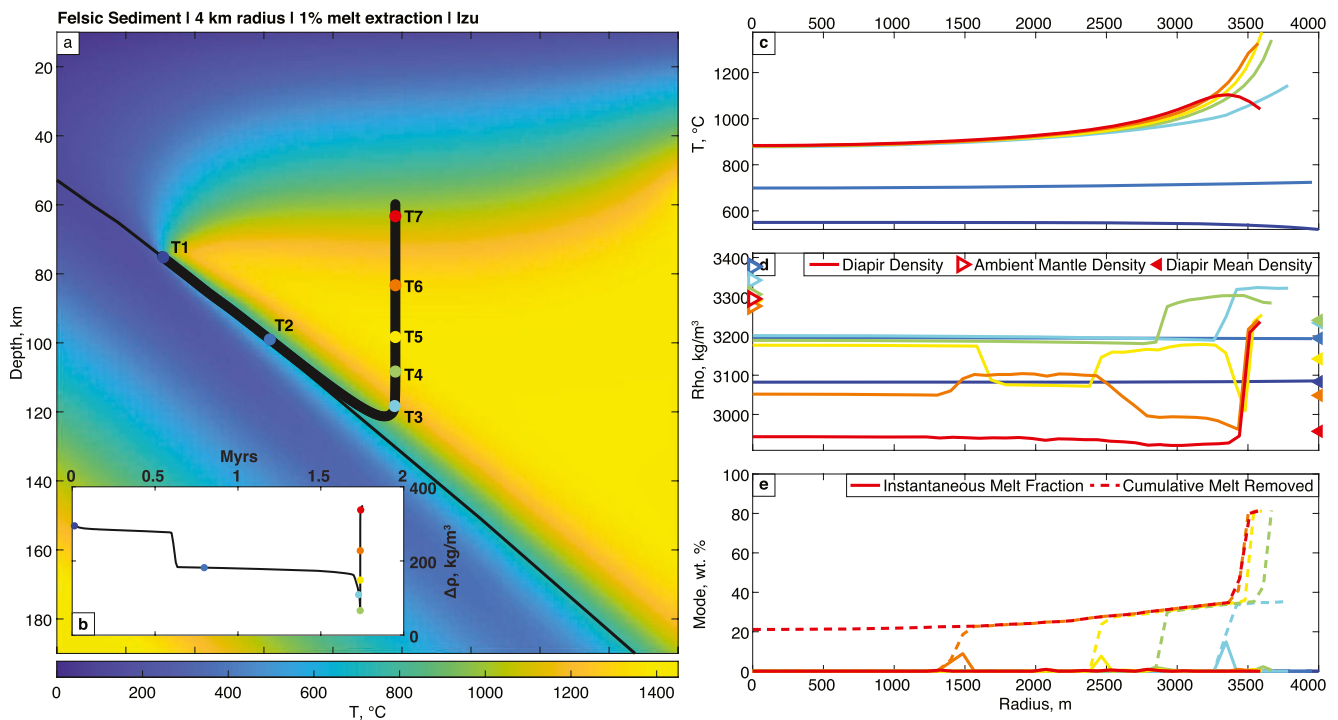


Figure 6. Behavior of 4-km felsic sediment diapir in Izu (cold arc) with 1% melt extraction threshold. (a) Diapir path superimposed on subduction zone thermal model, with specific time steps shown in subsequent panels and discussed in text marked. Slab top surface shown with medium black line. (b) Evolution of diapir buoyancy, that is, density difference (ambient mantle—bulk diapir), as a function of model time. (c) Radial profiles of diapir temperature. Individual lines show diapir temperatures at matching color time steps marked in panel (a) with matching color. (d) Radial profiles of diapir density, with colors as in panel (c). Open triangles along left axis show ambient mantle density at same time steps, while closed triangles on right axis show mean diapir density. (e) Radial profiles of melt fraction. Solid lines show instantaneous melt fractions, dashed lines show total cumulative melt fraction. Colors as in panel (c). Movie of this model available in the Supporting Information.

averaged all properties at each node by calculating Perple_X properties at intermediate 1-m intervals between nodes assuming a linear temperature gradient between nodes (following Hsiao [1985] and Comini et al. [1990]). This averaging assures that sudden jumps in material properties that occur between nodes are properly resolved. Following convergence in the thermal equation, melt fractions are calculated at each node, and if melt fractions above the extraction threshold are present, all melt is removed from that node and the composition and mass are updated. Finally, the total radius of the diapir and the nodal spacing is updated to reflect the change in density and any melt extraction, and the bulk density of the diapir is calculated for use in the next advection step.

4. Diapir Model Results

To illustrate the range of diapir behaviors predicted by our coupled phase equilibria-geodynamic model, we first describe two illustrative examples: (a) a 4-km radius diapir composed of intermediate sediment in Izu (cold subduction zone endmember) with 1% melt extraction, which results in relamination; and (b) a 4-km radius diapir composed of mafic sediment in Cascadia (hot subduction zone endmember) with 1% melt extraction, which produces an initially buoyant diapir that becomes negatively buoyant after melt is extracted and sinks back to the subducting slab. Following these detailed examples, we summarize the results of 168 total simulations to examine in detail the effect of each parameter on diapir behavior.

4.1. Model Examples

4.1.1. Intermediate Sediment Diapir With 4-km Radius in Izu

We first examine the evolution of a 4-km radius intermediate sediment diapir in Izu (Figure 6; an animated version of this figure is included in Supporting Information as Movie S1). At model initialization (T1),

the diapir is seeded 100 m above the slab surface at 75 km depth, and initially is thermally equilibrated with the surrounding mantle at $\sim 575^{\circ}\text{C}$ (Figures 6a and 6b). While the bulk diapir density at this stage is $< 3,100 \text{ kg/m}^3$ and thus is nearly 300 kg/m^3 less dense than the ambient mantle (Figure 6c), the cold slab surface conditions result in high mantle viscosities, and the diapir buoyancy velocity is much smaller than the background mantle velocity. Thus, initially the diapir remains coupled to the slab surface and is dragged downward by the plate motion. As the diapir is carried to greater depths along the slab surface (T2) it crosses the quartz-coesite boundary and the diapir density increases to $\sim 3,200 \text{ kg/m}^3$; $\sim 200 \text{ kg/m}^3$ less than the sub-arc mantle.

As the diapir continues to subduct, the slab top temperatures increase, mantle viscosity decreases, and the diapir begins to rise above the slab surface due to increasing buoyancy-driven velocity. When the diapir reaches $\sim 120 \text{ km}$ depth, its behavior changes markedly: the surrounding mantle at this stage has warmed to $\sim 850^{\circ}\text{C}$ and mantle viscosity has significantly decreased. As a result, the buoyancy-driven velocity component increases rapidly, and the path of the diapir becomes nearly vertical (Figure 6). This ascent path rapidly transports the diapir into significantly hotter mantle, and the outer rim of the diapir crosses the solidus (T3). This initial phase of phengite-breakdown melting produces $\sim 30\%$ melt, which is immediately extracted from the diapir (Figure 6d). Following melt extraction, the density of the melt-depleted region of the diapir increases to $\sim 3,300 \text{ kg/m}^3$. However, the bulk density of the diapir is $\sim 3,220 \text{ kg/m}^3$ and thus the diapir remains positively buoyant during its ascent through the mantle wedge. As the diapir continues to warm, the melting front migrates progressively inward (T4). At this stage, the diapir is rising extremely rapidly through the hot core of the mantle wedge ($\sim 10 \text{ s of m/yr}$). This rate is significantly faster than the thermal diffusion timescales within the diapir, producing large thermal gradients within the diapir.

As pressure decreases, the diapir passes back across the quartz/coesite transition (T5), and eventually crosses out of the jadeite stability field, stabilizing feldspar. Crossing each of these boundaries causes the diapir density to decrease, which counteracts the increase in density that occurs as the high-temperature rim of the now refractory diapir begins to melt again (T6). The model terminates with the diapir relaminating residual material to the base of the upper plate lithosphere (T7).

4.1.2. Mafic Sediment Diapir With 4-km Radius in Cascadia

Our second example examines a 4-km radius diapir composed of mafic sediment in the Cascadia subduction system (Figure 7, animated version available in Supporting Information as Movie S2). The evolution of this diapir diverges from the previous example almost immediately. Slab top temperatures in Cascadia are significantly higher than in Izu (Figure 5a), and as a result, the diapir rapidly warms immediately upon model initialization (T1, Figures 7a and 7b). The diapir is initially buoyant relative to the ambient mantle (Figure 7c) and the relatively high mantle temperatures lead to low viscosities, resulting in a large buoyancy-driven velocity component. The diapir quickly decouples from the slab top, and begins to ascend into the hot corner of the mantle wedge at only 80 km depth (T2 and T3). As the diapir passes through the steep thermal gradient above the slab, it rapidly heats and crosses the solidus. As in the previous example, an initial pulse of dehydration melting migrates into the core of the diapir, producing $\sim 25\%$ melt that is rapidly extracted, leaving a refractory, anhydrous bulk composition (Figure 7d).

Following this initial melting, the behavior of the diapir changes drastically. The residue formed after melting the mafic sediment bulk composition is nearly neutrally buoyant relative to the ambient mantle. As a result, the buoyancy-driven component of the diapir velocity decreases significantly and the diapir becomes entrained in the mantle corner flow (T4). The diapir is advected in this flow back toward the slab surface, while also continuing to heat in the hot core of the wedge, resulting in further melting. However, as the diapir is carried back toward the slab top it begins to cool, and high-temperature dry melting ceases before reaching the core of the diapir. After the cessation of melting, the diapir continues to cool and increase in density as it descends toward the slab top, becoming significantly denser than the ambient mantle (T5). As a result of this negative buoyancy and our simplified treatment of slab rheology, the diapir slowly sinks into the slab as it descends deeper into the mantle.

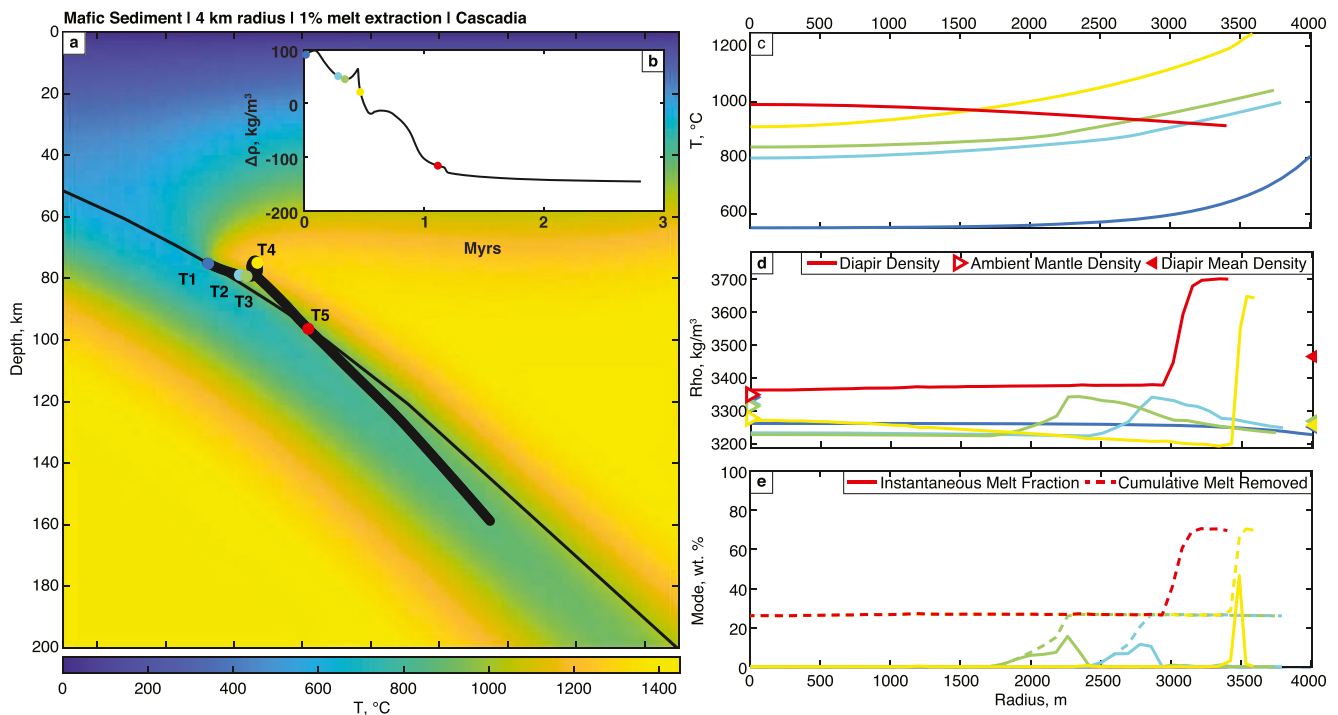


Figure 7. Behavior of 4-km mafic sediment diapir in Cascadia (warm arc) with 1% melt extraction. Figure components as in Figure 6. Movie of this model available in the Supporting Information.

4.2. Parameters Controlling Diapir Behavior

We next summarize the paths followed by diapirs in Alaska (a moderate temperature subduction zone) with each of the three representative compositions and varying radii from 1–3 km (Figure 8). In addition, we show how the path of each of these diapirs changes with different assumed melt extraction thresholds.

4.2.1. Diapir Radius

For all three representative compositions, a 1-km radius diapir never generates sufficiently large buoyancy-driven velocity to decouple from the slab surface and is instead carried beyond the subduction zone along the slab top (Figures 8a, 8d, and 8g). However, as diapir radius increases (rows in Figure 8) the depth to which a diapir descends on the slab top before transitioning to buoyancy-dominated near vertical flow decreases.

This highlights the critical control that radius (and by extension subducting sediment layer thickness) exerts on diapir behavior. The power-law form of the Stokes equation has a strong dependence on radius, and therefore larger radius diapirs transition to buoyancy dominated flow more rapidly, and also transit the mantle wedge more quickly than smaller diapirs. In addition, with increasing radius the thermal diffusion timescale of diapir increases. Therefore, the cores of larger diapirs heat and melt more slowly than the cores smaller diapirs. As melt extraction always results in increased bulk diapir density, this effectively delays the onset of negative buoyancy. Both of these effects make diapirism and ultimately relamination more likely as diapir radius increases.

4.2.2. Diapir Composition

As discussed in Section 2, diapir buoyancy is strongly sensitive to composition. We illustrate this effect by comparing the paths of diapirs composed of each of the three representative sediment types (Figure 8). As sediment composition becomes more felsic and the diapir buoyancy increases, diapirs form at shallower depths and ascend through the mantle wedge. Thus, all of the 2-km diapirs composed of felsic sediments successfully relaminate (Figure 8b), while none of the 2-km mafic sediment diapirs decouple from the slab top (Figure 8h). Similarly, all intermediate and felsic composition 3-km diapirs relaminate (Figures 8c and 8f),

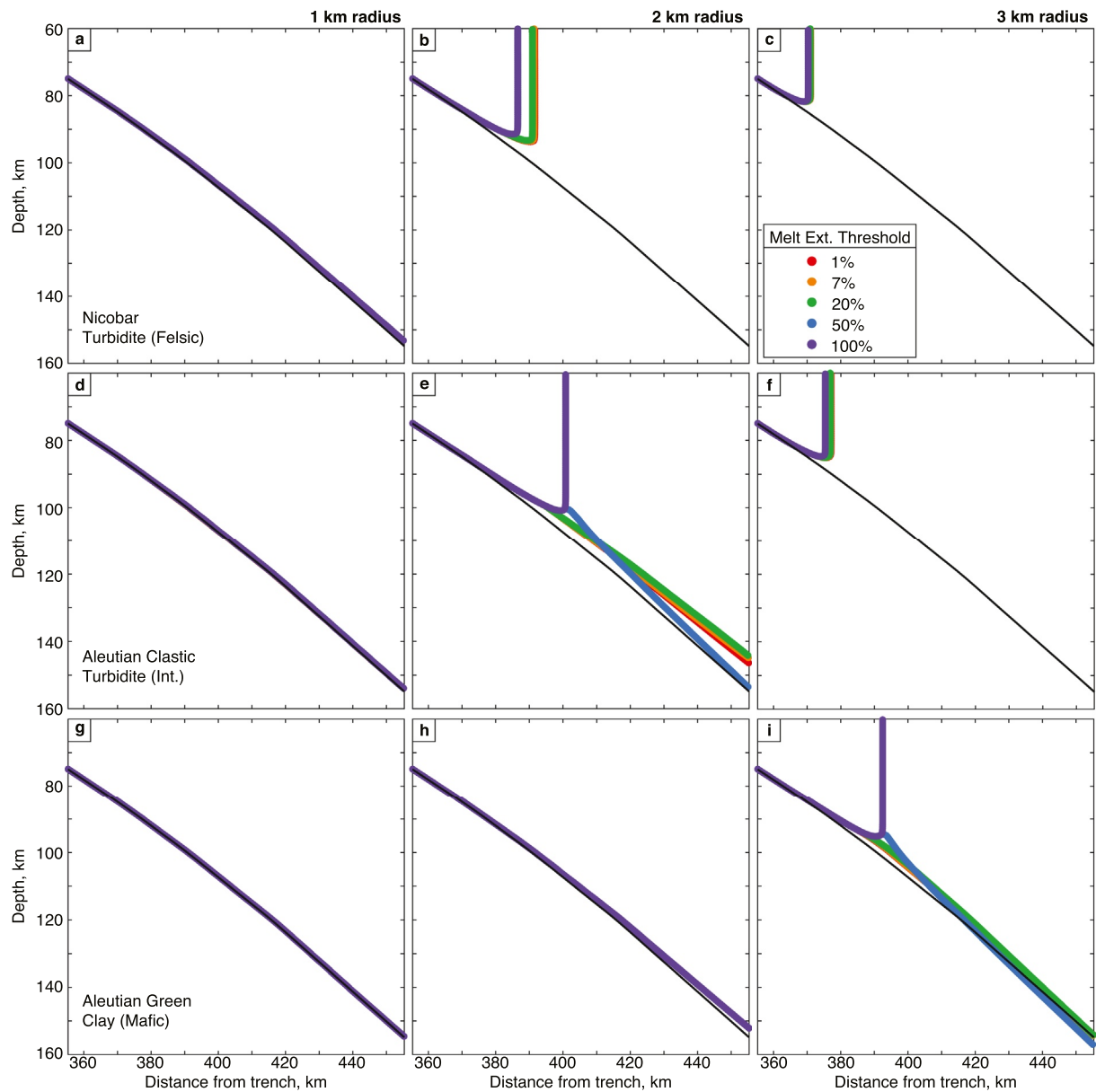


Figure 8. Modeled diapir paths using Alaskan (intermediate temperature) thermal model. Each panel contains five paths, with colors corresponding to melt extraction threshold. Each row of panels shows behavior of diapirs with a fixed initial composition with increasing radius. Scales for vertical and horizontal axes are equal and constant in all panels.

while only a subset of the mafic diapirs do (see following section). The importance of composition and diapir radius are of comparable magnitude for the conditions considered here. Thus, transitioning from mafic to intermediate compositions has a roughly equivalent effect to increasing the radius of the diapir by 1-km.

4.2.3. Melt Extraction Threshold

In principle, increasing the melt extraction threshold will increase the diapir buoyancy, as melt is less dense than the residual solid assemblage. Moreover, removing melt mass causes the diapir radius to decrease, while retaining melt counters this effect and further enhances diapir buoyancy. However, we note that there is an exception to this general behavior as closed-system melt production above phengite breakdown continues without the plateau in melt productivity that occurs in the fractional melting case. As a result, in cases with intermediate melt extraction thresholds, if melting continues above the solidus before reaching

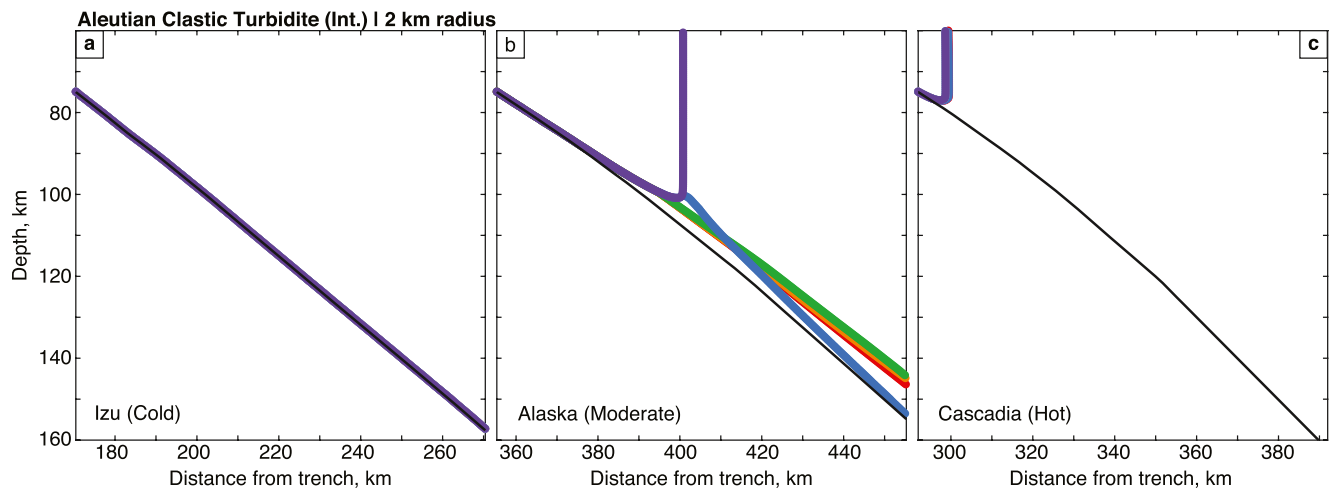


Figure 9. Variations in diapir model results for simulations using Izu Bonin (cold arc), Alaska (moderate temperature arc), and Cascadia (hot arc) subduction zone thermal models. Colors as in Figure 8.

the extraction threshold, the residues can become negatively buoyant at significantly lower temperatures than in analogous cases with lower melt extraction thresholds (Figures 3 and 5).

Overall, the melt extraction threshold appears to have a secondary control on diapir ascent compared to diapir radius and composition: for most combinations of radius and composition, changing the melt extraction threshold has a negligible impact. However, these effects are occasionally more pronounced. In particular, for the 2-km intermediate and the 3-km mafic cases (Figures 8e and 8i), diapir behavior differs notably as a function of the melt extraction threshold. For extraction thresholds between 1% and 20%, the near-solidus melt production is >20%; thus, the diapir loses significant melt and does not retain sufficient buoyancy to decouple from the slab top. By contrast, the 50% extraction case shows a different behavior: the diapir initially decouples from the slab as melt is retained, but as the diapir heats further and melting continues, it passes the 50% threshold, melt escapes, and the diapir becomes negatively buoyant. Although the 50% melt extraction scenario is perhaps an unlikely threshold to occur in the real world, we include it here to illustrate the range of possible behaviors. Given the interplay between diapir radius and melt extraction, it seems likely that similar loss of buoyancy could occur for lower melt extraction thresholds for diapirs with slightly larger radii (Figure 8). Finally, the closed system case is always buoyant and relaminates.

4.2.4. Subduction Zone Thermal Structure

The final parameter we investigated was the thermal state of the subduction zone (Figure 9). In these cases, all diapirs have a 2-km radius and intermediate sediment compositions, however, their behaviors differ greatly. Although the intermediate sediment is initially buoyant relative to the overlying mantle, diapirs in Izu (a cold subduction zone) remain coupled to the slab top and are carried beyond sub-arc depths without crossing the solidus (Figure 9a). By contrast, diapirism is increasingly favored in warmer subduction zones. In the moderate temperature case of the Alaskan subduction zone model, diapirs nucleate and decouple (Figure 9b). However, following melt extraction all diapirs except the closed system example become negatively buoyant and descend back to the slab, and only the diapir with no melt extraction is relaminated. Finally, in the hot subduction Cascadia example, all diapirs decouple from the slab and ascend rapidly through the wedge until they are re-emplated at the base of the plate (Figure 9c). In summary, the influence of subduction zone thermal structure on diapir evolution appears to be comparable in magnitude to changes in radius or composition. For example, a change from cold-to-intermediate or intermediate-to-hot subduction zones is roughly similar to increasing the radius of the diapir by 1 km.

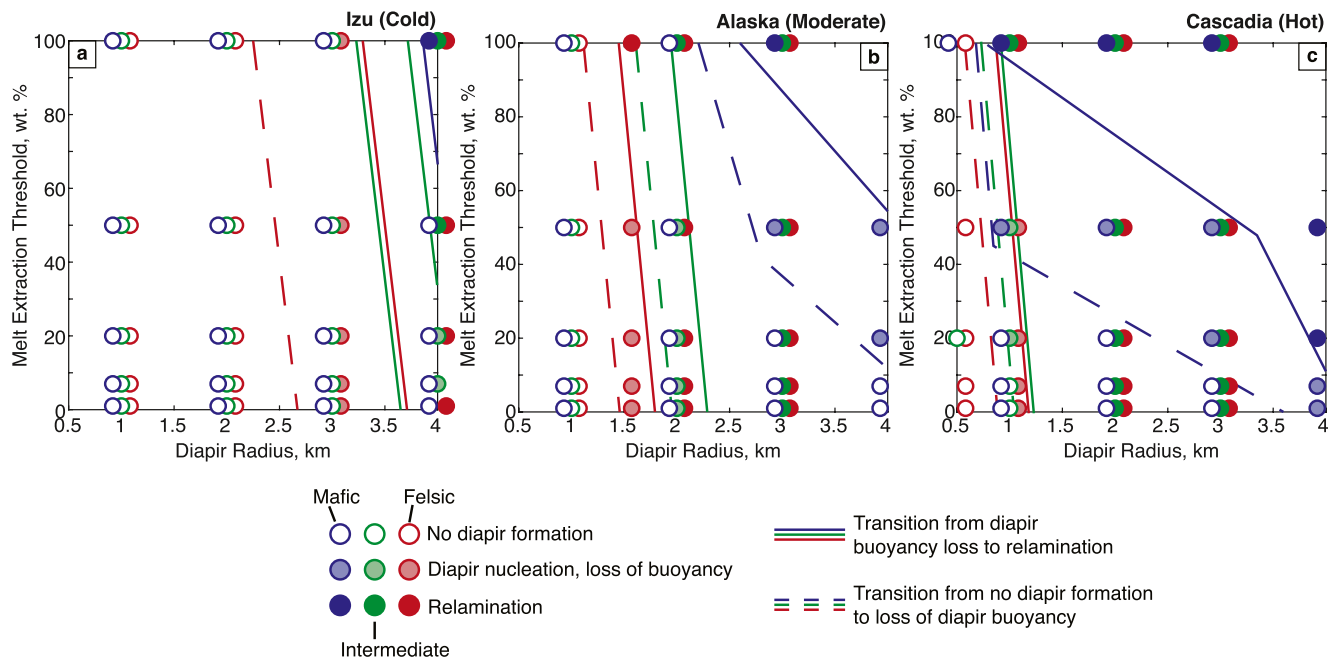


Figure 10. Regime diagrams characterizing the behavior of diapirs as a function of melt extraction threshold and diapir radius. Each symbol represents a single numerical experiment for diapirs composed of mafic (blue symbols), intermediate (green), and felsic (red) sediment. Transitions between fields where diapirs do not decouple and where diapirs form, but do not relaminate, are marked with dashed lines. Solid lines mark transition to field where relamination occurs.

5. Discussion

5.1. What Are the Dominant Controls on Sediment Diapir Behavior?

To summarize our modeling results, we develop a series of regime diagrams that divide the behavior of diapirs into three modes for each subduction zone thermal structure: (a) diapirs that never decouple from the slab top; (b) diapirs that decouple, ascend through the mantle wedge and relaminate to the upper plate; and (c) diapirs that ascend at least 5 km above the slab surface but do not relaminate (Figure 10). In detail, this third category includes two distinct behaviors: scenarios where the diapir is initially buoyant and then sinks back to the slab following melt extraction (as in Figure 7); and diapirs that ascend above the slab top but do not transition to the buoyancy-dominated regime such that the diapir is still advected downward with the slab out of the modeled domain.

For any given subduction zone, the three representative compositions smoothly transition between the three modes of diapir behavior (Figure 10). Moreover, the behavior of each composition varies consistently: the felsic composition transitions to forming diapirs and relaminating at the smallest radii, followed by the intermediate composition and finally the mafic composition. Similarly, there is a systematic variation due to subduction zone thermal structure: the cold subduction zone limits diapir relamination to only the largest radii (Figure 10a), while diapirs in the hot subduction zone relaminate at almost all radii (Figure 10c).

As discussed above, the melt extraction threshold has a smaller effect on diapir behavior compared to composition and radius. The one exception is for the mafic sediment composition, which exhibits the greatest change in density following melt extraction, and thus is much more sensitive to this variable. In particular, the mafic sediment composition remains positively buoyant in the equilibrium melting case with no melt extraction. In this scenario, any mafic diapir that decouples from the slab top will inevitably relaminate. By contrast, lower melt extraction thresholds for the mafic sediment are likely to produce an initially buoyant diapir that sinks back to the slab after the onset of melting and melt extraction. For these smaller melt extraction thresholds, mafic diapirs will only relaminate if they are sufficiently large to ascend through the mantle without fully thermally equilibrating and melting. This phenomenon is well-illustrated in the Cascadia regime diagram (Figure 10c), where the behaviors in mafic sediment are separated by much shallower slopes compared to the other compositions.

By comparison, the intermediate composition is generally much less dense than the mafic composition and only becomes negatively buoyant after high degrees of melting at very high temperatures. As a result, the regime where diapir melting causes loss of buoyancy is restricted. Finally, the felsic composition is nearly always buoyant relative to the mantle, regardless of the melt extraction threshold. The non-relamination mode for the felsic composition is thus limited to cases where the diapir has not fully decoupled from the slab within the model domain. However, because these diapirs likely remain positively buoyant even at greater depths, it is likely that they will eventually decouple from the slab and ascend from greater depths in the back-arc region.

5.2. Sediment Diapirs as an Arc Differentiation Mechanism?

As discussed above, a range of behaviors is predicted for subducted sediments in different subduction settings. In all but the coldest subduction zones, felsic sediment diapirs larger than ~ 2 km are expected to relaminate. By contrast, only the largest radii mafic sediment diapirs relaminate. These differences in behavior suggest that subducted sediment diapirism may be an efficient process for the differentiation of arc crust, in which more felsic subducted material is preferentially returned to arc crust via relamination (cf., Kelemen & Behn, 2016). This process may be relevant within single subduction systems if the subducted sediment thickness is large enough that diapirs can form preferentially from the most felsic material, or more likely, is a process that primarily differs between subduction zones, where diapir formation and relamination are more common in subduction zones that subduct more felsic sediments.

We expand the regime diagram in Figure 10 to highlight that this differentiation process is not only possible, but that it may be highly efficient for “typical” subduction zones (Figure 11). Specifically, differentiation by relamination is inefficient at the coldest subduction zones, where for almost all reasonable sediment thicknesses diapirs are unlikely to decouple from the slab. Similarly, at the hottest subduction zones, a wide range of sediment compositions will form diapirs and even relaminate, suggesting that while the mass flux of relaminated material may be large, it is less likely to be compositionally sorted. In contrast to these two end member cases, the evolution of sediment diapirs in moderate temperature subduction zones is strongly controlled by sediment composition. In these settings, felsic sediment diapirs with radii greater than 1.5 km will relaminate, while intermediate composition diapirs only relaminate at radii >2.5 km, and mafic diapirs are not expected to relaminate for any reasonable thickness of subducting sediments.

5.3. Application to Global Subduction Zones

These results show that, for the range of subduction zones and sediment compositions and thicknesses present today, a variety of sediment behaviors can be expected. To better quantify the distribution of processes affecting subducted sediments in modern subduction zones, we constructed models representative of 15 modern subduction zones. These models each use locally calculated thermal models from van Keken et al. (2018), modified as described in Section 3.2, and use locally estimated average subducted sediment compositions (Plank & Langmuir, 1998) and thicknesses (Clift et al., 2009). To conservatively account for uncertainty in sediment thicknesses due to both sediment accretion and forearc erosion, we also varied diapir radius in each subduction zone by a factor of 2.

We predict that sediment diapirs relaminate in five modern subduction zones (filled circles in Figure 12), while in 10 other subduction zones, we find that the diapirs do not decouple from the downgoing slab (open circles in Figure 12). The behavior of the five relamination subduction zones (Southern Chile, Alaska, Sunda, Cascadia, and Nankai) is unchanged even while varying the sediment thickness by a factor of 2, suggesting that this finding is relatively robust. By contrast, three of the subduction zones (Aleutians, Northeast Japan, Kamchatka) that do not decouple are relatively close to the transition between behaviors, and in these cases doubling the sediment thickness causes a shift to relamination. While our above analysis shows that sediment thickness, composition, and subduction zone all have important controls on diapir behavior, it appears that diapir radius (as estimated from subducting sediment layer thickness) is the dominant control in modern systems. For the modern subduction zones examined here, relamination almost always occurs when diapir radii are greater than ~ 2.5 km, and is never observed in smaller radii simulations. By contrast,

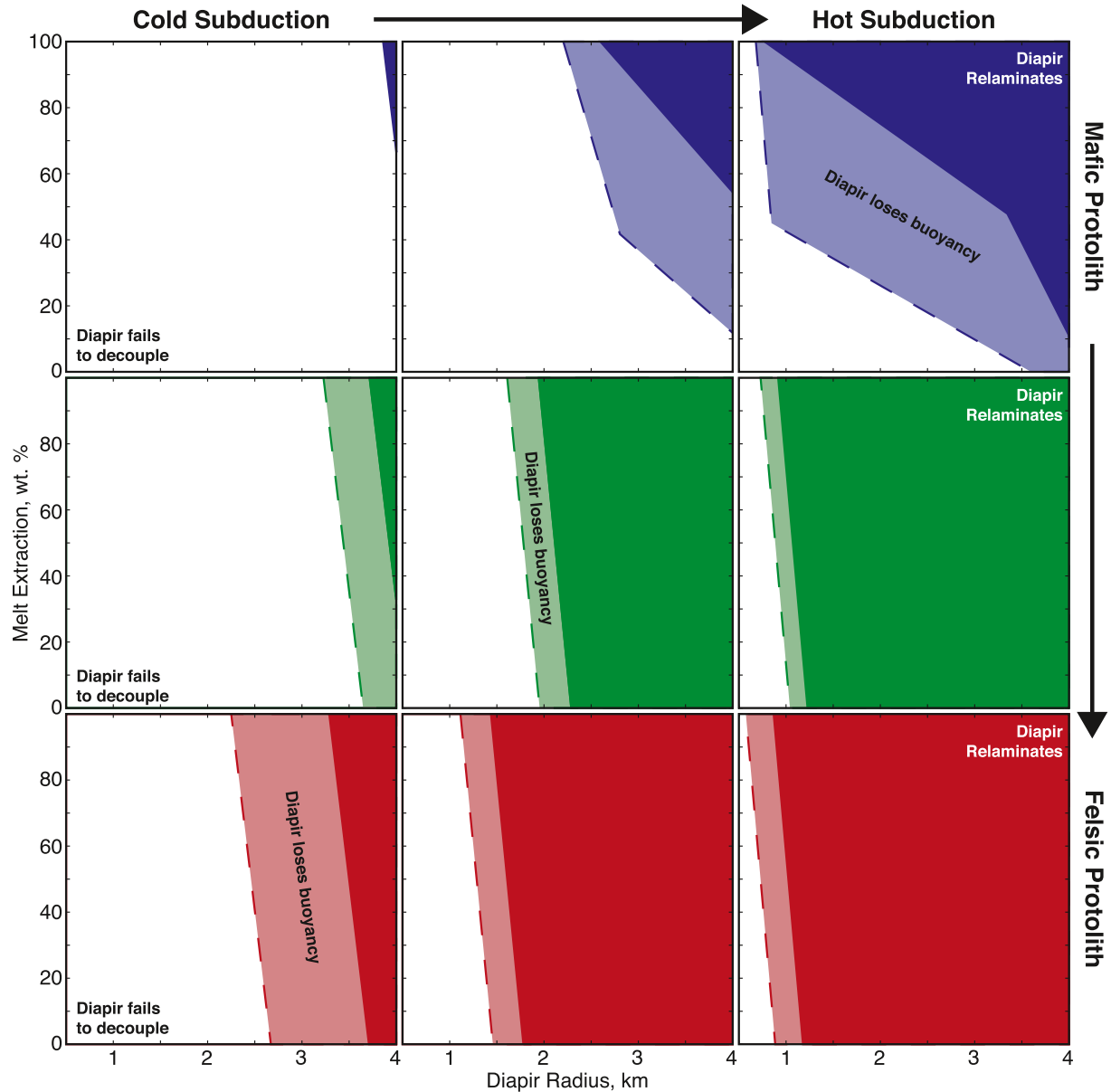


Figure 11. Grid of regime diagrams showing the systematic variation in subducted sediment diapirs as a function of sediment composition and subduction zone thermal state.

some of the lowest density diapirs do not decouple (e.g., Marianas), and diapirs also do not decouple in some of the warmest subduction zones (e.g., Mexico).

We also find that, at least in the arcs considered, relamination appears to be far more common in modern continental arcs than in island arcs. All five of the relamination cases are continental arcs. By contrast, based on the estimated sediment thicknesses, relamination does not occur in any island arc system, although relamination is predicted in the Aleutians if the sediment thickness is doubled. This variation is the result of continental arcs dominantly subducting thicker sediment layers, and is not the result of variations in sediment density. These continental arcs with thick trench sediment layers are dominantly accretionary margins and thus the estimated sediment thicknesses may be overestimates compared to the volume of material transported to the mantle wedge. However, we find that relamination still occurs in these five arcs even if the sediment volume is reduced by 50%, a reduction greater than long-term estimates of accretion rates (Clift & Vannucchi, 2004). This suggests an intriguing feedback with regards to continent construction,

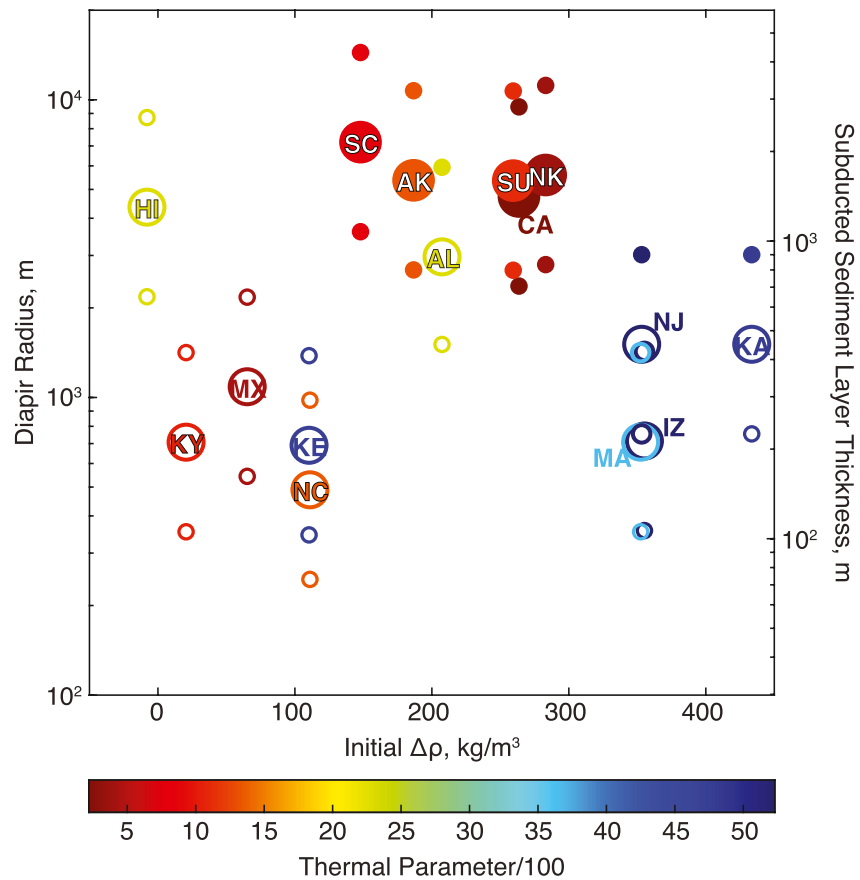


Figure 12. Summary of results from simulations for modern arcs based on the thermal structures of van Keken et al. (2018) with modified potential temperature as described in the text, using average trench sediment composition estimates from Plank and Langmuir (1998), and trench sediment estimates from Clift et al. (2009). Symbols as in Figure 10: filled symbols mark simulations that predict relamination, empty symbols show results where the diapir did not decouple from the downgoing slab. Larger labeled symbols show results using published sediment thicknesses, smaller symbols show results when varying thicknesses by a factor of 2 from the estimated value. Initial density difference ($\Delta\rho$) values are calculated at model initiation, and symbols are colored by arc thermal parameter (product of slab descent velocity and plate age). Arc abbreviations: AK—Alaska; AL—Aleutians; CA—Cascadia; HI—Hikurangi; IZ—Izu Bonin; KA—Kamchatka; Ke—Kermadec; KY—Kyushu; MA—Marianas; MX—Mexico; NC—North Chile; NJ—Northern Japan; NK—Nankai; SC—South Chile; SU—Sunda.

wherein arcs that appear to be more efficiently destroying continental material through sediment subduction are also the locations where relamination is most likely to occur. Finally, we stress that this result does not imply relamination never occurs in island arcs. In addition to the Aleutians case, the southern Lesser Antilles are an island arc where subducting sediment layers are likely thick enough to drive relamination based on the regime diagram in Figure 11 (the Lesser Antilles arc was not modeled in Figure 12 due to the lack of a site-specific thermal model).

5.4. Identification of Relaminated Sediments

This analysis raises the question of how prevalent sediment relamination is on Earth today. If subducted sediments are readily returned to the base of arc crust at many continental arcs, we might expect more abundant evidence of this process. However, unequivocal instances of relaminated material have to date proved elusive. We emphasize that relaminated material will be emplaced within arc lower crust (Kelemen & Behn, 2016), rather than exhumed to shallower depths within the subduction channel. Thus, the presence of UHP materials within arc lower crust alone is a compelling observation in support of relamination (e.g., Yin et al., 2007). Unfortunately, this same fact provides an explanation for the difficulty in identifying

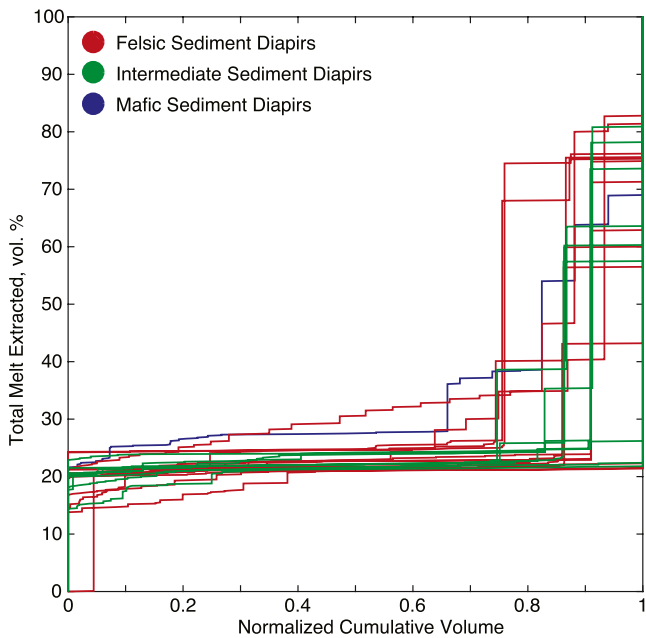


Figure 13. Extracted melt fractions in all diapir simulations that result in relamination. Relative proportions of melt volumes are consistent regardless of composition, subduction zone, and melt extraction—between 70% and 80% of the relaminated diapir has lost 20%–30% melt, while the remaining (outermost) diapir volume loses significantly greater melt fractions.

relaminated materials: exposures of arc lower crust are quite limited globally (Ducea et al., 2015). Further, the storage of relaminated material within still active, relative warm, arc lower crust will likely produce a granulite facies overprint, obscuring any diagnostic UHP record. Indeed, such overprinting would cause relaminated material to appear similarly in outcrop to more typical felsic orthogneisses, which are common in arc lower crust (Kelemen & Behn, 2016). Moreover, any structural features diagnostic of diapirism will likely be overprinted during emplacement within the comparatively rigid arc crust and subsequent arc magmatism (cf., Gerya et al., 2006).

On the other hand, our modeling suggests a number of features unique to relamination that may prove more enduring. The rapid vertical velocities predicted for most diapirs (tens of meters per year) transiting the hot core of the mantle wedge is a feature unique to this process. Larger decompression rates (at least 100 m/yr) have been calculated for UHP rocks from the Saxonian Erzgebirge in the Bohemian Massif based on the large differential pressures required to drive brittle decrepitation of fluid inclusions in garnet at UHP conditions (Stockert et al., 2009). This observation was originally taken as evidence that the Erzgebirge samples ascended as crystal-bearing magma (Stockert et al., 2009), but is equally consistent with diapiric ascent in the presence of relatively low degrees of retained melt. A perhaps more broadly identifiable feature produced during the rapid ascent of sediment diapirs is an extremely sharp thermal gradient within the diapir, as the thermal diffusion timescale within the diapir is much longer than the ascent timescale. As mentioned above, the temperature record of this thermal disequilibrium may not be preserved; however, strong thermal gradients would also lead to large differences in

the extent of melting within a diapir (Figure 13). Regardless of diapir size, composition, and thermal setting, nearly all diapir simulations that produced relamination show a common melting systematic: the interior of the diapir, comprising ~70%–90% of the total volume, records absolute melt extractions of 20–30 vol%, while the remaining outermost material records significantly higher degrees of melt extraction from 50% to 70%. Thus, observations of significant variations in the extent of melt depletion across km-scale areas within the UHP Kokchetav Massif in Kazakhstan (Stepanov et al., 2014) and in near-UHP xenoliths erupted in the Pamir (Hacker et al., 2005) may be evidence of relaminated material in these locations.

5.5. Limitations of Our Diapir Model?

While the thermodynamic model employed in our diapir model utilizes the best available experimental data, other aspects of the model are built on a number of simplifying assumptions. The importance of these assumptions, and their impact on our conclusions warrant further discussion. In particular, we discuss below the importance of three key assumptions in our dynamic model: (a) the nucleation phase of diapir formation, (b) the absence of external fluids, and (c) our choice of sediment compositions.

5.5.1. Diapir Nucleation and Ascent

One major simplification to our approach is the treatment of diapirs as a buoyant tracer within the mantle wedge. This simplification results in a two-stage behavior in many models, where the diapir is initially coupled to the slab top, and is transported at near plate velocities down-dip, followed by a buoyancy-driven stage, where the diapir ascends near vertically through mantle wedge with velocities that are orders of magnitude greater than plate velocities. The first stage, where the diapir is coupled to the slab, effectively corresponds to the interval where diapirs initially nucleate as instabilities from the subducted sediment layer (e.g., Behn et al., 2011; Miller & Behn, 2012). While we do not explicitly model this process here, we note that the behavior of the diapirs in our models, and the transition from coupled plate driven velocities to buoyancy driven ascent is broadly consistent with models for the behavior of diapirs during nucleation (Miller & Behn, 2012). Specifically, the transition from background strain-rate controlled mantle viscosity

to buoyancy-driven mantle viscosity, which coincides with the transition to buoyancy-driven ascent, is comparable to the transition from exponential to super-exponential diapir formation described by Miller and Behn (2012). Thus, while we do not directly model diapir nucleation, our modeling approach is consistent with the dynamics of this process.

The behavior of the diapir during this initial coupled stage is controlled by both the slab top temperatures and the background strain rate. Our assumed background strain rate of 10^{-13} s^{-1} is consistent with both the kinematic-dynamic models employed here and with previous diapir nucleation studies (Miller & Behn, 2012; van Keken et al., 2018), but is near the high end of previous estimates. Decreasing the background strain rate hinders the initial process where diapirs separate from the slab, and carries the diapirs to greater depths in the mantle before they transition to buoyancy dominated flow (Figure S3 in Supporting Information S1). Decreasing the background strain rate to 10^{-14} s^{-1} or 10^{-15} s^{-1} has a comparable effect to changes in subduction zone thermal structure. Thus, while lower background strain rates may reduce the formation of small radius diapirs, felsic and intermediate diapirs are still likely to form in warm to hot subduction zones. At these lower strain rates, arc crust differentiation by diapir relamination is likely to persist, and may become more efficient as fewer subduction zones will produce diapirs that relaminate for a wide range of compositions as is modeled in Cascadia.

Finally, during the ascent of diapirs through the mantle wedge, our model predicts remarkably fast velocities on the order of tens of meters per year. While these velocities are significantly greater than subduction velocities, we note that they are similar to previous modeling work (Yin et al., 2007) and are consistent with diapir velocity estimates from both analog experiments (Hall & Kincaid, 2001) and fully dynamic models (Larsen & Yuen, 1997a, 1997b). These very rapid ascent velocities may also be consistent with isotopic disequilibria data that require transfer of material from the slab to the surface within hundreds to thousands of years (Turner et al., 2001).

5.5.2. Fluid-Saturated Melting

An additional assumption that underlies our approach is that there is unlikely to be an external fluid source to the diapirs, and thus fluid-absent initial conditions are most relevant. This is likely to be true once a diapir nucleates and begins to ascend through the mantle wedge. However, as discussed above, in most cases there is an initial stage where the diapir either has not yet nucleated, or has not significantly separated from the slab interface. During this stage, it is possible that the diapir material would be fluxed by fluids derived from dehydrating material further down-dip on the slab (e.g., van Keken et al., 2011; Wada et al., 2012). In this scenario, fluid-saturated conditions will be present and the diapir material will begin to melt during this initial stage before reaching the temperatures necessary to rapidly ascend into the mantle wedge. While we do not model this scenario, we can speculate here on the implications of initial wet melting for diapir behavior.

Under a wet melting scenario, nearly all modern subduction zones slab tops cross the solidus between 2 and 3 GPa, where the solidus temperatures range from ~ 650 to 700°C (Figure 5a; Mann & Schmidt, 2015). This initial near-solidus melt is granitic (Schmidt, 2015), and melt productivity near the solidus will be controlled by the quantity of excess fluid present (Mann & Schmidt, 2015). Similarly, the interval above the solidus where phengite remains stable is a function of bulk sediment composition and available fluid, but generally can extend to $\sim 900^\circ\text{C}$ at 3 GPa (Mann & Schmidt, 2015). If this wet-melting stage is near fractional, a refractory residue will be produced if phengite breaks down, limiting further melting (Zhang et al., 2020).

Thus, we speculate that the evolution of sediment diapirs formed from initially fluid-saturated material may not differ significantly from what we have modeled, and specifically that the density maps shown in Figure 5 for depleted residues will likely be broadly similar to the residues produced by lower temperature wet melting. If so, the ability of mafic sediments to generate diapirs would be significantly curtailed, as this composition rapidly becomes negatively buoyant following small extents of melting. By contrast, intermediate and felsic sediments should remain buoyant and form diapirs even following low to moderate extents of fluid-present melting on the slab top. The subsequent evolution of these diapirs will be dictated by the presence of phengite in the residue compositions. If phengite is stable, the diapir will experience an initial phengite-breakdown fluid-absent melting interval as it ascends into hotter mantle. On the other hand, if sufficient wet melting has occurred to remove all phengite, the diapir will be anhydrous and will not melt further until reaching the hot core of the mantle wedge.

5.5.3. Compositional Variations

In contrast to the sediment diapirs explored here, it has also been suggested that diapirs may form either from *mélange* composed of a mix of sediment, MORB, and hydrated peridotite (e.g., Marschall & Schumacher, 2012), or even from hydrated peridotite alone (e.g., Gerya & Yuen, 2003). While we have not modeled these compositions directly, our results still provide insight into these processes. While a range of relatively less dense, hydrous phases may be present in these lithologies, amphibole and serpentine both breakdown prior to the temperatures required for diapir nucleation (Poli & Schmidt, 2002). Therefore, *mélange* diapirs are likely to consist of sediment + chlorite-rich hydrated peridotite. As chlorite has significantly lower density than mantle ($\sim 2,800 \text{ kg/m}^3$) and is stable to $\sim 850^\circ\text{C}$ at 3 GPa (Pawley, 2003), these lithologies would likely contribute to diapir formation. However, the chlorite in these *mélange* diapirs will breakdown rapidly as the diapir ascends into the hotter portions of the mantle wedge, resulting in a dense anhydrous residue that is unlikely to relaminate. Formation of diapirs that melt and subsequently become negatively buoyant and sink into the deeper mantle may be more likely to result in these systems (Codillo et al., 2018; Nielsen & Marschall, 2017).

Finally, we note that while the thermodynamic model we employed necessitated the exclusion of carbonate-rich sediments, the viability of diapir formation in these types of sediments has important implications for subduction zone carbon budgets (e.g., Kelemen & Manning, 2015). The density of typical carbonates (calcite, aragonite, dolomite) at 3–5 GPa ranges from 2,800 to 3,100 kg/m^3 (calculated with Abers and Hacker [2016]), lower than the densities of many of the sediment compositions considered here (e.g., Figures 6 and 7). Therefore, the presence of carbonates in subducted sediments will likely both encourage diapir nucleation and increase the buoyancy of sediment diapirs. Moreover, the presence of carbonate increases the fluid-saturated solidus temperature by only $\sim 50^\circ\text{C}$ and has a negligible effect on the fluid-absent solidus (Mann & Schmidt, 2015; Tsuno & Dasgupta, 2012). As a result, the melting behavior in carbonate-bearing sediments will not significantly affect the results discussed above for CO_2 -free compositions. Based on these observations, we suggest that carbonate-bearing sediments are likely to form diapirs that transfer melt and CO_2 -rich fluids to the surrounding mantle wedge and may be relaminated to the base of arc crust.

6. Conclusion

In this study, we re-calibrated a melt *a-X* model to accurately reproduce melting reactions in sediments at sub-arc mantle pressures and temperatures. Using this model, we show that most sediment compositions will be buoyant relative to ambient mantle at slab-top conditions, and further that dehydration melting is unlikely to occur in most sediment compositions at typical slab-top conditions. We integrated this modified thermodynamic model into a coupled phase equilibria-dynamic model of sediment diapirs. Our coupled model shows that diapir formation and behavior within the mantle wedge is strongly sensitive to multiple variables including sediment composition, diapir radius (which is controlled by subducted sediment thicknesses), slab top geotherms, and finally, melt extraction thresholds.

Our modeling shows that the full range of hypothesized sediment processes can be produced by the present range of sediment compositions and subduction zones. Warmer subduction zones with slower slab velocities or shallower slab dips favor the formation of diapirs at sub-arc depths. Thicker sediment layers composed of more felsic material also favor diapir formation, and these larger, more buoyant diapirs are more likely to relaminate, regardless of melt extraction. We find that sediment diapir relamination is likely to occur at a number of modern continental arcs, even if a significant portion of trench sediments are accreted or underthrust to the upper plate at shallower depths. By contrast, cold, steeply dipping subduction zones, and smaller subducted sediment thicknesses will hinder diapir formation, and in these settings sediment contributions will be limited to either wet-melting or fluid release on the slab top. Finally, based on our modeling, we highlight a number of observations that may be useful in identifying relaminated material in the field including: UHP mineral assemblages in arc lower crust; evidence for extremely rapid sediment exhumation; and strong gradients in either metamorphic temperature or extents of depletion over km length scales.

Data Availability Statement

All necessary matlab code used for diapir simulations presented in this study are available for download from figshare at <https://doi.org/10.6084/m9.figshare.16896544.v1>. No new data were created or used during this research.

Acknowledgments

This study was supported by NSF grants EAR-18-52680 and EAR-18-55430 and funding from Boston College. The authors thank Ikuko Wada for rerunning and sharing the modified subduction zone models, and Veronique Le Roux for helpful discussion relating to this study. This manuscript was improved by thoughtful and detailed reviews from A. Smye and an anonymous reviewer, as well as suggestions from the associate editor W. Behr.

References

- Abers, G. A., & Hacker, B. R. (2016). A MATLAB toolbox and Excel workbook for calculating the densities, seismic wave speeds, and major element composition of minerals and rocks at pressure and temperature. *Geochemistry, Geophysics, Geosystems*, 17(2), 616–624. <https://doi.org/10.1002/2015GC006171>
- Agard, P., Plunder, A., Angiboust, S., Bonnet, G., & Ruh, J. (2018). The subduction plate interface: Rock record and mechanical coupling (from long to short timescales). *Lithos*, 320–321, 537–566. <https://doi.org/10.1016/j.lithos.2018.09.029>
- Agard, P., Yamato, P., Jolivet, L., & Burov, E. (2009). Exhumation of oceanic blueschists and eclogites in subduction zones: Timing and mechanisms. *Earth-Science Reviews*, 92(1–2), 53–79. <https://doi.org/10.1016/j.earscirev.2008.11.002>
- Auzanneau, E., Vielzeuf, D., & Schmidt, M. W. (2006). Experimental evidence of decompression melting during exhumation of subducted continental crust. *Contributions to Mineralogy and Petrology*, 152(2), 125–148. <https://doi.org/10.1007/s00410-006-0104-5>
- Bassett, D., Sutherland, R., Henrys, S., Stern, T., Scherwath, M., Benson, A., et al. (2010). Three-dimensional velocity structure of the northern Hikurangi margin, Raukumara, New Zealand: Implications for the growth of continental crust by subduction erosion and tectonic underplating. *Geochemistry, Geophysics, Geosystems*, 11(10). <https://doi.org/10.1029/2010GC003137>
- Behn, M. D., Kelemen, P. B., Hirth, G., Hacker, B. R., & Massonne, H. J. (2011). Diapirs as the source of the sediment signature in arc lavas. *Nature Geoscience*, 4(9), 641–646. <https://doi.org/10.1038/ngeo1214>
- Burov, E., Jaupart, C., & Guillou-Frottier, L. (2003). Ascent and emplacement of buoyant magma bodies in brittle-ductile upper crust. *Journal of Geophysical Research: Solid Earth*, 108(B4). <https://doi.org/10.1029/2002JB001904>
- Castro, A., & Gerya, T. V. (2008). Magmatic implications of mantle wedge plumes: Experimental study. *Lithos*, 103(1–2), 138–148. <https://doi.org/10.1016/j.lithos.2007.09.012>
- Castro, A., Vogt, K., & Gerya, T. V. (2013). Generation of new continental crust by sublithospheric silicic-magma relamination in arcs: A test of Taylor's andesite model. *Gondwana Research*, 23(4), 1554–1566. <https://doi.org/10.1016/j.gr.2012.07.004>
- Chapman, T., Clarke, G. L., & Daczko, N. R. (2019). The role of buoyancy in the fate of ultra-high-pressure eclogite. *Scientific Reports*, 9. <https://doi.org/10.1038/s41598-019-56475-y>
- Chatterjee, N., & Jagoutz, O. (2015). Exhumation of the UHP Tso Moriri eclogite as a diapir rising through the mantle wedge. *Contributions to Mineralogy and Petrology*, 169(1), 1–20. <https://doi.org/10.1007/s00410-014-1099-y>
- Chauvel, C., Lewin, E., Carpentier, M., Arndt, N. T., & Marini, J. C. (2007). Role of recycled oceanic basalt and sediment in generating the Hf-Nd mantle array. *Nature Geoscience*, 1(1), 64–67. <https://doi.org/10.1038/ngeo.2007.51>
- Chauvel, C., Marini, J. C., Plank, T., & Ludden, J. N. (2009). Hf-Nd input flux in the Izu-Mariana subduction zone and recycling of subducted material in the mantle. *Geochemistry, Geophysics, Geosystems*, 10(1). <https://doi.org/10.1029/2008GC002101>
- Clift, P. D., & Hartley, A. J. (2007). Slow rates of subduction erosion and coastal underplating along the Andean margin of Chile and Peru. *Geology*, 35(6), 503–506. <https://doi.org/10.1130/G23584A.1>
- Clift, P. D., Schouten, H., & Vannucchi, P. (2009). Arc-continent collisions, sediment recycling and the maintenance of the continental crust. *Geological Society, London, Special Publications*, 318(1), 75–103. <https://doi.org/10.1144/SP318.3>
- Clift, P. D., & Vannucchi, P. J. (2004). Controls on tectonic accretion versus erosion in subduction zones: Implications for the origin and recycling of the continental crust. *Reviews of Geophysics*, 42(2). <https://doi.org/10.1029/2003RG000127>
- Codillo, E. A., Le Roux, V., & Marschall, H. R. (2018). Arc-like magmas generated by mélange-peridotite interaction in the mantle wedge. *Nature Communications*, 9(1). <https://doi.org/10.1038/s41467-018-05313-2>
- Comini, G., Del Giudice, S., & Saro, O. (1990). A conservative algorithm for multidimensional conduction phase change. *International Journal for Numerical Methods in Engineering*, 30(4), 697–709. <https://doi.org/10.1002/nme.1620300410>
- Connolly, J. A. D. (2005). Computation of phase equilibria by linear programming: A tool for geodynamic modeling and its application to subduction zone decarbonation. *Earth and Planetary Science Letters*, 236(1–2), 524–541. <https://doi.org/10.1016/j.epsl.2005.04.033>
- Connolly, J. A. D. (2009). The geodynamic equation of state: What and how. *Geochemistry, Geophysics, Geosystems*, 10(10). <https://doi.org/10.1029/2009GC002540>
- Cruz-Urbe, A. M., Marschall, H. R., Gaetani, G. A., & Le Roux, V. (2018). Generation of alkaline magmas in subduction zones by partial melting of mélange diapirs—An experimental study. *Geology*, 46(4), 343–346. <https://doi.org/10.1130/G39956.1>
- Currie, C. A., Beaumont, C., & Huisman, R. S. (2007). The fate of subducted sediments: A case for backarc intrusion and underplating. *Geology*, 35(12), 1111–1114. <https://doi.org/10.1130/G24098A.1>
- Ducea, M. N., Saleeby, J. B., & Bergantz, G. (2015). The architecture, chemistry, and evolution of continental magmatic arcs. *Annual Review of Earth and Planetary Sciences*, 43(1), 299–331. <https://doi.org/10.1146/annurev-earth-060614-105049>
- Elliott, T., Plank, T., Zindler, A., White, W., & Bourdon, B. (1997). Element transport from slab to volcanic front at the Mariana arc. *Journal of Geophysical Research: Solid Earth*, 102(B7), 14991–15019. <https://doi.org/10.1029/97JB00788>
- Erdman, M. E., & Lee, C. T. A. (2014). Oceanic- and continental-type metamorphic terranes: Occurrence and exhumation mechanisms. *Earth-Science Reviews*, 139, 33–46. <https://doi.org/10.1016/j.earscirev.2014.08.012>
- Ernst, W. G., Hacker, B. R., & Liou, J. G. (2007). Petrotectonics of ultrahigh-pressure crustal and upper-mantle rocks—Implications for Phanerozoic collisional orogens. *Geological Society of America Special Papers*, 433, 27–49. [https://doi.org/10.1130/2007.2433\(02\)](https://doi.org/10.1130/2007.2433(02))
- Gerya, T. V., Connolly, J. A. D., Yuen, D. A., Górczyk, W., & Capel, A. M. (2006). Seismic implications of mantle wedge plumes. *Physics of the Earth and Planetary Interiors*, 156(1–2), 59–74. <https://doi.org/10.1016/j.pepi.2006.02.005>
- Gerya, T. V., Stöckhert, B., & Perchuk, A. L. (2002). Exhumation of high-pressure metamorphic rocks in a subduction channel: A numerical simulation. *Tectonics*, 21(6), 6–16. <https://doi.org/10.1029/2002TC001406>
- Gerya, T. V., & Yuen, D. A. (2003). Rayleigh-Taylor instabilities from hydration and melting propel “cold plumes” at subduction zones. *Earth and Planetary Science Letters*, 212(1–2), 47–62. [https://doi.org/10.1016/S0012-821X\(03\)00265-6](https://doi.org/10.1016/S0012-821X(03)00265-6)

- Gómez-Tuena, A., Cavazos-Tovar, A. M., Parolari, M., Straub, S. M., & Espinasa-Perena, R. (2018). Geochronological and geochemical evidence of continental crust "relamination" in the origin of intermediate arc magmas. *Lithos*, 322(3–4), 52–66. <https://doi.org/10.1016/j.lithos.2018.10.005>
- Green, E. C. R., Holland, T., & Powell, R. (2007). An order-disorder model for omphacitic pyroxenes in the system jadeite-diopside-hedenbergite-acmite, with applications to eclogitic rocks. *American Mineralogist*, 92(7), 1181–1189. <https://doi.org/10.2138/am.2007.2401>
- Green, E. C. R., White, R. W., Diener, J. F. A., Powell, R., Holland, T. J. B., & Palin, R. M. (2016). Activity-composition relations for the calculation of partial melting equilibria in metabasic rocks. *Journal of Metamorphic Geology*, 34(9), 845–869. <https://doi.org/10.1111/jmg.12211>
- Guillot, S., Hattori, K., Agard, P., Schwartz, S., & Vidal, O. (2009). Exhumation processes in oceanic and continental subduction contexts: A review. In S. Lallemand & F. Funicello (Eds.), *Subduction zone geodynamics. Frontiers in Earth Sciences* (pp. 175–205). Springer. https://doi.org/10.1007/978-3-540-87974-9_10
- Hacker, B. R. (2008). H₂O subduction beyond arcs. *Geochemistry, Geophysics, Geosystems*, 9(3). <https://doi.org/10.1029/2007GC001707>
- Hacker, B. R., Kelemen, P. B., & Behn, M. D. (2011). Differentiation of the continental crust by relamination. *Earth and Planetary Science Letters*, 307(3–4), 501–516. <https://doi.org/10.1016/j.epsl.2011.05.024>
- Hacker, B. R., Luffi, P., Lutkov, V., Minaev, V., Ratschbacher, L., Plank, T., et al. (2005). Near-ultrahigh pressure processing of continental crust: Miocene crustal xenoliths from the Pamir. *Journal of Petrology*, 46(8), 1661–1687. <https://doi.org/10.1093/ptrology/egi030>
- Hall, P. S., & Kincaid, C. (2001). Diapiric flow at subduction zones: A recipe for rapid transport. *Science*, 292(5526), 2472–2475. <https://doi.org/10.1126/science.1060488>
- Hasenclever, J., Morgan, J. P., Hort, M., & Rüpke, L. H. (2011). 2D and 3D numerical models on compositionally buoyant diapirs in the mantle wedge. *Earth and Planetary Science Letters*, 311(1–2), 53–68. <https://doi.org/10.1016/j.epsl.2011.08.043>
- Hawkesworth, C. J., Turner, S. P., McDermott, F., Peate, D. W., & van Calsteren, P. (1997). U-Th isotopes in arc magmas: Implications for element transfer from the subducted crust. *Science*, 276(5312), 551–555. <https://doi.org/10.1126/science.276.5312.551>
- Hermann, J., & Spandler, C. J. (2008). Sediment melts at sub-arc depths: An experimental study. *Journal of Petrology*, 49(4), 717–740. <https://doi.org/10.1093/ptrology/egm073>
- Herzberg, C., Asimow, P. D., Arndt, N., Niu, Y., Leshner, C. M., Fitton, J. G., et al. (2007). Temperatures in ambient mantle and plumes: Constraints from basalts, picrites, and komatiites. *Geochemistry, Geophysics, Geosystems*, 8(2). <https://doi.org/10.1029/2006GC001390>
- Hirth, G., & Kohlstedt, D. (2003). Rheology of the upper mantle and the mantle wedge: A view from the experimentalists. In J. Eiler (Ed.), *Inside the subduction factory. Geophysical Monograph Series* (Vol. 138, pp. 83–105). American Geophysical Union. <https://doi.org/10.1029/138GM06>
- Holland, T., & Powell, R. (2003). Activity–composition relations for phases in petrological calculations: An asymmetric multicomponent formulation. *Contributions to Mineralogy and Petrology*, 145(4), 492–501. <https://doi.org/10.1007/s00410-003-0464-z>
- Holland, T. J. B., Green, E. C. R., & Powell, R. (2018). Melting of peridotites through to granites: A simple thermodynamic model in the system KNCFMASHTOCr. *Journal of Petrology*, 59(5), 881–900. <https://doi.org/10.1093/ptrology/egy048>
- Horleston, A. C., & Helffrich, G. R. (2012). Constraining sediment subduction: A converted phase study of the Aleutians and Marianas. *Earth and Planetary Science Letters*, 359–360, 141–151. <https://doi.org/10.1016/j.epsl.2012.10.019>
- Houseman, G. A., & Molnar, P. (1997). Gravitational (Rayleigh-Taylor) instability of a layer with non-linear viscosity and convective thinning of continental lithosphere. *Geophysical Journal International*, 128(1), 125–150. <https://doi.org/10.1111/j.1365-246x.1997.tb04075.x>
- Hsiao, J. S. (1985). An efficient algorithm for finite-difference analyses of heat transfer with melting and solidification. *Numerical Heat Transfer*, 8(6), 653–666. <https://doi.org/10.1080/01495728508961877>
- Jagoutz, O., & Kelemen, P. B. (2015). Role of arc processes in the formation of continental crust. *Annual Review of Earth and Planetary Sciences*, 43(1), 363–404. <https://doi.org/10.1146/annurev-earth-040809-152345>
- Johnson, M. C., & Plank, T. (1999). Dehydration and melting experiments constrain the fate of subducted sediments. *Geochemistry, Geophysics, Geosystems*, 1(12). <https://doi.org/10.1029/1999GC000014>
- Jull, M., & Kelemen, P. B. (2001). On the conditions for lower crustal convective instability. *Journal of Geophysical Research: Solid Earth*, 106(B4), 6423–6446. <https://doi.org/10.1029/2000JB900357>
- Kelemen, P. B., & Behn, M. D. (2016). Formation of lower continental crust by relamination of buoyant arc lavas and plutons. *Nature Geoscience*, 9(3), 197–205. <https://doi.org/10.1038/ngeo2662>
- Kelemen, P. B., & Manning, C. E. (2015). Reevaluating carbon fluxes in subduction zones, what goes down, mostly comes up. *Proceedings of the National Academy of Sciences of the United States of America*, 112(30), E3997–E4006. <https://doi.org/10.1073/pnas.1507889112>
- Klemme, S., Blundy, J. D., & Wood, B. J. (2002). Experimental constraints on major and trace element partitioning during partial melting of eclogite. *Geochimica et Cosmochimica Acta*, 66(17), 3109–3123. [https://doi.org/10.1016/S0016-7037\(02\)00859-1](https://doi.org/10.1016/S0016-7037(02)00859-1)
- Kusbach, V., Janoušek, V., Hasalová, P., Schulmann, K., Fanning, C. M., Erban, V., & Ulrich, S. (2015). Importance of crustal relamination in origin of the orogenic mantle peridotite–high-pressure granulite association: Example from the Náměšť Granulite Massif (Bohemian Massif, Czech Republic). *Journal of the Geological Society*, 172(4), 479–490. <https://doi.org/10.1144/jgs2014-070>
- Larsen, T. B., & Yuen, D. A. (1997a). Fast plumeheads: Temperature-dependent versus non-Newtonian rheology. *Geophysical Research Letters*, 24(16), 1995–1998. <https://doi.org/10.1029/97GL01886>
- Larsen, T. B., & Yuen, D. A. (1997b). Ultrafast upwelling bursting through the upper mantle. *Earth and Planetary Science Letters*, 146(3–4), 393–399. [https://doi.org/10.1016/S0012-821X\(96\)00247-6](https://doi.org/10.1016/S0012-821X(96)00247-6)
- Lin, C. H., Shih, M. H., & Lai, Y. C. (2019). A strong seismic reflector within the mantle wedge above the Ryukyu subduction of Northern Taiwan. *Seismological Research Letters*, 91(1), 310–316. <https://doi.org/10.1785/0220190174>
- Lin, C. H., Shih, M. H., & Lai, Y. C. (2021). Mantle wedge diapirs detected by a dense seismic array in Northern Taiwan. *Scientific Reports*, 11(1), 1–12. <https://doi.org/10.1038/s41598-021-81357-7>
- Little, T. A., Hacker, B. R., Gordon, S. M., Baldwin, S. L., Fitzgerald, P. G., Ellis, S., & Korchinski, M. (2011). Diapiric exhumation of Earth's youngest (UHP) eclogites in the gneiss domes of the D'Entrecasteaux Islands, Papua New Guinea. *Tectonophysics*, 510(1–2), 39–68. <https://doi.org/10.1016/j.tecto.2011.06.006>
- Maierová, P., Schulmann, K., & Gerya, T. V. (2018). Relamination styles in collisional orogens. *Tectonics*, 37(1), 224–250. <https://doi.org/10.1002/2017TC004677>
- Mann, U., & Schmidt, M. W. (2015). Melting of pelitic sediments at subarc depths: 1. Flux vs. fluid-absent melting and a parameterization of melt productivity. *Chemical Geology*, 404, 150–167. <https://doi.org/10.1016/j.chemgeo.2015.02.032>
- Manning, C. E. (2018). Fluids of the lower crust: Deep is different. *Annual Review of Earth and Planetary Sciences*, 46(1), 67–97. <https://doi.org/10.1146/annurev-earth-060614-105224>

- Marschall, H. R., & Schumacher, J. C. (2012). Arc magmas sourced from mélange diapirs in subduction zones. *Nature Geoscience*, 5(12), 862–867. <https://doi.org/10.1038/ngeo1634>
- Maunder, B., van Hunen, J., Magni, V., & Bouilhol, P. (2016). Relamination of mafic subducting crust throughout Earth's history. *Earth and Planetary Science Letters*, 449, 206–216. <https://doi.org/10.1016/j.epsl.2016.05.042>
- Meneghini, F., Marroni, M., Moore, J. C., Pandolfi, L., & Rowe, C. D. (2009). The processes of underthrusting and underplating in the geologic record: Structural diversity between the Franciscan Complex (California), the Kodiak Complex (Alaska) and the Internal Ligurian Units (Italy). *Geological Journal*, 44(2), 126–152. <https://doi.org/10.1002/gj.1144>
- Miller, N. C., & Behn, M. D. (2012). Timescales for the growth of sediment diapirs in subduction zones. *Geophysical Journal International*, 190(3), 1361–1377. <https://doi.org/10.1111/j.1365-246X.2012.05565.x>
- Morris, J. D., Gosse, J., Brachfeld, S., & Tera, F. (2002). Cosmogenic Be-10 and the solid Earth: Studies in geomagnetism, subduction zone processes, and active tectonics. *Reviews in Mineralogy and Geochemistry*, 50(1), 207–270. <https://doi.org/10.2138/rimg.2002.50.5>
- Nabelek, P. I., Whittington, A. G., & Hofmeister, A. M. (2010). Strain heating as a mechanism for partial melting and ultrahigh temperature metamorphism in convergent orogens: Implications of temperature-dependent thermal diffusivity and rheology. *Journal of Geophysical Research: Solid Earth*, 115(B12). <https://doi.org/10.1029/2010JB007727>
- Nichols, G. T., Wyllie, P. J., & Stern, C. R. (1994). Subduction zone melting of pelagic sediments constrained by melting experiments. *Nature*, 371(6500), 785–788. <https://doi.org/10.1038/371785a0>
- Nielsen, S. G., Horner, T. J., Pryer, H. V., Blusztajn, J., Shu, Y., Kurz, M. D., & Le Roux, V. (2018). Barium isotope evidence for pervasive sediment recycling in the upper mantle. *Science Advances*, 4(7). <https://doi.org/10.1126/sciadv.aas8675>
- Nielsen, S. G., & Marschall, H. R. (2017). Geochemical evidence for mélange melting in global arcs. *Science Advances*, 3(4). <https://doi.org/10.1126/sciadv.1602402>
- Nielsen, S. G., Shu, Y., Auro, M., Yogodzinski, G., Shinjo, R., Plank, T., et al. (2020). Barium isotope systematics of subduction zones. *Geochimica et Cosmochimica Acta*, 275, 1–18. <https://doi.org/10.1016/j.gca.2020.02.006>
- Nielsen, S. G., Yogodzinski, G., Prytulak, J., Plank, T., Kay, S. M., Kay, R. W., et al. (2016). Tracking along-arc sediment inputs to the Aleutian arc using thallium isotopes. *Geochimica et Cosmochimica Acta*, 181, 217–237. <https://doi.org/10.1016/j.gca.2016.03.010>
- Patiño-Douce, A. E. (2005). Vapor-absent melting of tonalite at 15–32 kbar. *Journal of Petrology*, 46(2), 275–290. <https://doi.org/10.1093/ptrology/egh071>
- Pawley, A. (2003). Chlorite stability in mantle peridotite: The reaction clinocllore+enstatite=forsterite+pyrope+H₂O. *Contributions to Mineralogy and Petrology*, 144(4), 449–456. <https://doi.org/10.1007/s00410-002-0409-y>
- Plank, T. (2005). Constraints from thorium/lanthanum on sediment recycling at subduction zones and the evolution of the continents. *Journal of Petrology*, 46(5), 921–944. <https://doi.org/10.1093/ptrology/egi005>
- Plank, T., & Langmuir, C. H. (1993). Tracing trace elements from sediment input to volcanic output at subduction zones. *Nature*, 362(6422), 739–743. <https://doi.org/10.1038/362739a0>
- Plank, T., & Langmuir, C. H. (1998). The chemical composition of subducting sediment and its consequences for the crust and mantle. *Chemical Geology*, 145(3–4), 325–394. [https://doi.org/10.1016/S0009-2541\(97\)00150-2](https://doi.org/10.1016/S0009-2541(97)00150-2)
- Poli, S., & Schmidt, M. W. (2002). Petrology of subducted slabs. *Annual Review of Earth and Planetary Sciences*, 30(1), 207–235. <https://doi.org/10.1146/annurev.earth.30.091201.140550>
- Rapp, R. P., Irifune, T., Shimizu, N., Nishiyama, N., Norman, M. D., & Inoue, T. (2008). Subduction recycling of continental sediments and the origin of geochemically enriched reservoirs in the deep mantle. *Earth and Planetary Science Letters*, 271(1–4), 14–23. <https://doi.org/10.1016/j.epsl.2008.02.028>
- Rehkämper, M., & Hofmann, A. W. (1997). Recycled ocean crust and sediment in Indian Ocean MORB. *Earth and Planetary Science Letters*, 147(1–4), 93–106. [https://doi.org/10.1016/S0012-821X\(97\)00009-5](https://doi.org/10.1016/S0012-821X(97)00009-5)
- Riker-Coleman, K. E., Gallup, C. D., Wallace, L. M., Webster, J. M., Cheng, H., & Edwards, R. L. (2006). Evidence of Holocene uplift in east New Britain, Papua New Guinea. *Geophysical Research Letters*, 33(18). <https://doi.org/10.1029/2006GL026596>
- Ringwood, A. E. (1979). *Origin of the Earth and Moon*. Springer.
- Rosenberg, C. L., & Handy, M. R. (2005). Experimental deformation of partially melted granite revisited: Implications for the continental crust. *Journal of Metamorphic Geology*, 23(1), 19–28. <https://doi.org/10.1111/j.1525-1314.2005.00555.x>
- Schmidt, M. W. (2015). Melting of pelitic sediments at subarc depths: 2. Melt chemistry, viscosities and a parameterization of melt composition. *Chemical Geology*, 404, 168–182. <https://doi.org/10.1016/j.chemgeo.2015.02.013>
- Schmidt, M. W., & Jagoutz, O. (2017). The global systematics of primitive arc melts. *Geochemistry, Geophysics, Geosystems*, 18(8), 2817–2854. <https://doi.org/10.1002/2016GC006699>
- Schmidt, M. W., Vielzeuf, D., & Auzanneau, E. (2004). Melting and dissolution of subducting crust at high pressures: The key role of white mica. *Earth and Planetary Science Letters*, 228(1–2), 65–84. <https://doi.org/10.1016/j.epsl.2004.09.020>
- Scholl, D. W. (2019). Seismic imaging evidence that forearc underplating built the accretionary rock record of coastal North and South America. *Geological Magazine*, 158(1), 104–117. <https://doi.org/10.1017/S0016756819000955>
- Scholl, D. W., & von Huene, R. (2007). Crustal recycling at modern subduction zones applied to the past—Issues of growth and preservation of continental basement crust, mantle geochemistry, and supercontinent reconstruction. In R. D. Hatcher Jr, M. P. Carlson, J. H. McBride, & J. R. Martínez Catalán (Eds.), *4-D Framework of continental crust*, *Geological Society of America Memoir* (Vol. 200, pp. 9–32). Geological Society of America. [https://doi.org/10.1130/2007.1200\(02\)](https://doi.org/10.1130/2007.1200(02))
- Scholl, D. W., & von Huene, R. (2009). Implications of estimated magmatic additions and recycling losses at the subduction zones of accretionary (non-collisional) and collisional (suturing) orogens. *Geological Society, London, Special Publications*, 318(1), 105–125. <https://doi.org/10.1144/SP318.4>
- Skora, S., & Blundy, J. D. (2010). High-pressure hydrous phase relations of radiolarian clay and implications for the involvement of subducted sediment in arc magmatism. *Journal of Petrology*, 51(11), 2211–2243. <https://doi.org/10.1093/ptrology/egq054>
- Skora, S., Blundy, J. D., Brooker, R. A., Green, E. C. R., de Hoog, J. C. M., & Connolly, J. A. D. (2015). Hydrous phase relations and trace element partitioning behaviour in calcareous sediments at subduction-zone conditions. *Journal of Petrology*, 56(5), 953–980. <https://doi.org/10.1093/ptrology/egv024>
- Spandler, C., Yaxley, G., Green, D. H., & Scott, D. (2010). Experimental phase and melting relations of metapelite in the upper mantle: Implications for the petrogenesis of intraplate magmas. *Contributions to Mineralogy and Petrology*, 160(4), 569–589. <https://doi.org/10.1007/s00410-010-0494-2>
- Stepanov, A. S., Hermann, J., Korsakov, A. V., & Rubatto, D. (2014). Geochemistry of ultrahigh-pressure anatexis: Fractionation of elements in the Kokchetav gneisses during melting at diamond-facies conditions. *Contributions to Mineralogy and Petrology*, 167(5). <https://doi.org/10.1007/s00410-014-1002-x>

- Stöckhert, B., Trepmann, C. A., & Massonne, H. J. (2009). Decrepitated UHP fluid inclusions: About diverse phase assemblages and extreme decompression rates (Erzgebirge, Germany). *Journal of Metamorphic Geology*, 27(9), 673–684. <https://doi.org/10.1111/j.1525-1314.2009.00835.x>
- Straub, S. M., Gómez-Tuena, A., & Vannucchi, P. (2020). Subduction erosion and arc volcanism. *Nature Reviews Earth & Environment*, 1(11), 574–589. <https://doi.org/10.1038/s43017-020-0095-1>
- Syracuse, E. M., van Keken, P. E., & Abers, G. A. (2010). The global range of subduction zone thermal models. *Physics of the Earth and Planetary Interiors*, 183(1–2), 73–90. <https://doi.org/10.1016/j.pepi.2010.02.004>
- Tewskbury-Christle, C. M., Behr, W. M., & Helper, M. A. (2021). Tracking deep sediment underplating in a fossil subduction margin: Implications for interface rheology and mass and volatile recycling. *Geochemistry, Geophysics, Geosystems*, 22(3). <https://doi.org/10.1029/2020GC009463>
- Till, C. B. (2017). A review and update of mantle thermobarometry for primitive arc magmas. *American Mineralogist*, 102(5), 931–947. <https://doi.org/10.2138/am-2017-5783>
- Tsuno, K., & Dasgupta, R. (2012). The effect of carbonates on near-solidus melting of pelite at 3 GPa: Relative efficiency of H₂O and CO₂ subduction. *Earth and Planetary Science Letters*, 319–320, 185–196. <https://doi.org/10.1016/j.epsl.2011.12.007>
- Turner, S., Evans, P., & Hawkesworth, C. (2001). Ultrafast source-to-surface movement of melt at island arcs from ²²⁶Ra-²³⁰Th systematics. *Science*, 292(5520), 1363–1366. <https://doi.org/10.1126/science.1059904>
- van Keken, P. E., Hacker, B. R., Syracuse, E. M., & Abers, G. A. (2011). Subduction factory: 4. Depth-dependent flux of H₂O from subducting slabs worldwide. *Journal of Geophysical Research: Solid Earth*, 116(B1). <https://doi.org/10.1029/2010JB007922>
- van Keken, P. E., Wada, I., Abers, G. A., Hacker, B. R., & Wang, K. (2018). Mafic high-pressure rocks are preferentially exhumed from warm subduction settings. *Geochemistry, Geophysics, Geosystems*, 19(9), 2934–2961. <https://doi.org/10.1029/2018GC007624>
- Vigneresse, J. L., Barbey, P., & Cuney, M. (1996). Rheological transitions during partial melting and crystallization with application to felsic magma segregation and transfer. *Journal of Petrology*, 37(6), 1579–1600. <https://doi.org/10.1093/petrology/37.6.1579>
- Voller, V. R., Swaminathan, C. R., & Thomas, B. G. (1990). Fixed grid techniques for phase change problems: A review. *International Journal for Numerical Methods in Engineering*, 30(4), 875–898. <https://doi.org/10.1002/nme.1620300419>
- Wada, I., Behn, M. D., & Shaw, A. M. (2012). Effects of heterogeneous hydration in the incoming plate, slab rehydration, and mantle wedge hydration on slab-derived H₂O flux in subduction zones. *Earth and Planetary Science Letters*, 353(354), 60–71. <https://doi.org/10.1016/j.epsl.2012.07.025>
- Wada, I., & Wang, K. (2009). Common depth of slab-mantle decoupling: Reconciling diversity and uniformity of subduction zones. *Geochemistry, Geophysics, Geosystems*, 10(10). <https://doi.org/10.1029/2009GC002570>
- Weinberg, R. F., & Podladchikov, Y. (1994). Diapiric ascent of magmas through power law crust and mantle. *Journal of Geophysical Research: Solid Earth*, 99(B5), 9543–9559. <https://doi.org/10.1029/93JB03461>
- White, R. W., Powell, R., Holland, T. J. B., Johnson, T. E., & Green, E. C. R. (2014). New mineral activity–composition relations for thermodynamic calculations in metapelitic systems. *Journal of Metamorphic Geology*, 32(3), 261–286. <https://doi.org/10.1111/jmg.12071>
- Yin, A., Manning, C. E., Lovera, O., Menold, C. A., Chen, X., & Gehrels, G. E. (2007). Early paleozoic tectonic and thermomechanical evolution of ultrahigh-pressure (UHP) metamorphic rocks in the Northern Tibetan Plateau, Northwest China. *International Geology Review*, 49(8), 681–716. <https://doi.org/10.2747/0020-6814.49.8.681>
- Zhang, N., Behn, M. D., Parmentier, E. M., & Kincaid, C. (2020). Melt segregation and depletion during ascent of buoyant diapirs in subduction zones. *Journal of Geophysical Research: Solid Earth*, 125(2). <https://doi.org/10.1029/2019JB018203>